Systems/Circuits

The Retinal Basis of Light Aversion in Neonatal Mice

Franklin S. Caval-Holme,[1] Marcos L. Aranda,[2] Andy Q. Chen,[3] Alexandre Tiriac,[3] Yizhen Zhang,[3] Benjamin Smith,[4] Lutz Birnbaumer,[5,6] Tiffany M. Schmidt,[2,7] and Marla B. Feller[1,3]

[1]Helen Wills Neuroscience Institute, University of California Berkeley, Berkeley, California 94720, [2]Department of Neurobiology, Northwestern University, Evanston, Illinois 60208, [3]Department of Molecular and Cell Biology, University of California Berkeley, Berkeley, California 94720, [4]School of Optometry, University of California Berkeley, Berkeley, California 94720, [5]Signal Transduction Laboratory, National Institute of Environmental Health Sciences, National Institutes of Health, Durham, North Carolina 27709, [6]Institute of Biomedical Research, School of Medical Sciences, Catholic University of Argentina, Buenos Aires, Argentina C1107AFF, and [7]Department of Ophthalmology, Northwestern University Feinberg School of Medicine, Chicago, Illinois 60611

Aversive responses to bright light (photoaversion) require signaling from the eye to the brain. Melanopsin-expressing intrinsically photosensitive retinal ganglion cells (ipRGCs) encode absolute light intensity and are thought to provide the light signals for photoaversion. Consistent with this, neonatal mice exhibit photoaversion before the developmental onset of image vision, and melanopsin deletion abolishes photoaversion in neonates. It is not well understood how the population of ipRGCs, which constitutes multiple physiologically distinct types (denoted M1-M6 in mouse), encodes light stimuli to produce an aversive response. Here, we provide several lines of evidence that M1 ipRGCs that lack the Brn3b transcription factor drive photoaversion in neonatal mice. First, neonatal mice lacking TRPC6 and TRPC7 ion channels failed to turn away from bright light, while two photon Ca^{2+} imaging of their acutely isolated retinas revealed reduced photosensitivity in M1 ipRGCs, but not other ipRGC types. Second, mice in which all ipRGC types except for Brn3b-negative M1 ipRGCs are ablated exhibited normal photoaversion. Third, pharmacological blockade or genetic knockout of gap junction channels expressed by ipRGCs, which reduces the light sensitivity of M2-M6 ipRGCs in the neonatal retina, had small effects on photoaversion only at the brightest light intensities. Finally, M1s were not strongly depolarized by spontaneous retinal waves, a robust source of activity in the developing retina that depolarizes all other ipRGC types. M1s therefore constitute a separate information channel between the neonatal retina and brain that could ensure behavioral responses to light but not spontaneous retinal waves.

Key words: connexin; Cx45; Cx30.2; development; enucleation; photocurrent

Significance Statement

At an early stage of development, before the maturation of photoreceptor input to the retina, neonatal mice exhibit photoaversion. On exposure to bright light, they turn away and emit ultrasonic vocalizations, a cue to their parents to return them to the nest. Neonatal photoaversion is mediated by intrinsically photosensitive retinal ganglion cells (ipRGCs), a small percentage of the retinal ganglion cell population that express the photopigment melanopsin and depolarize directly in response to light. This study shows that photoaversion is mediated by a subset of ipRGCs, called M1-ipRGCs. Moreover, M1-ipRGCs have reduced responses to retinal waves, providing a mechanism by which the mouse distinguishes light stimulation from developmental patterns of spontaneous activity.

Received Jan. 20, 2022; revised Mar. 9, 2022; accepted Mar. 15, 2022.

Author contributions: F.S.C.-H., M.L.A., A.Q.C., A.T., and M.B.F. designed research; F.S.C.-H., M.L.A., A.Q.C., A.T., Y.Z., and T.M.S. performed research; F.S.C.-H., M.L.A., A.Q.C., A.T., Y.Z., and T.M.S. analyzed data; F.S.C.-H., A.Q.C., and M.B.F. wrote the first draft of the paper; F.S.C.-H., M.L.A., A.Q.C., A.T., Y.Z., B.S., L.B., T.M.S., and M.B.F. edited the paper; F.S.C.-H., A.Q.C., and M.B.F. wrote the paper; M.L.A., A.T., B.S., L.B., and T.M.S. contributed unpublished reagents/analytic tools.

F.S.C.-H. was supported by National Institutes of Health (NEI) F31EY028022-03. M.B.F. and B.S. were supported by National Institutes of Health R01EY019498, National Institutes of Health R01EY013528, and National Institutes of Health P30EY003176. M.L.A. and T.M.S. were supported by National Institutes of Health (NEI) 1DP2EY027983. L.B. was supported by National Institutes of Health Intramural Research Program Project Z01-ES-101684. Confocal images were obtained on a microscope at the Molecular Imaging Center at UC Berkeley. Further information, requests for resources and reagents, and any additional information required to reanalyze the data reported in this paper should be directed to and will be fulfilled by the Lead Contact, Marla B. Feller (mfeller@berkeley.edu). We thank Michael Tri Hoang Do and members of the M.B.F. laboratory for comments on the manuscript. We would like to thank Karin Dedek for the generous gift of Cx30.2 mice.

The authors declare no competing financial interests.

Correspondence should be addressed to Marla B. Feller at mfeller@berkeley.edu.

https://doi.org/10.1523/JNEUROSCI.0151-22.2022

Introduction

Aversive responses to light in humans (Noseda et al., 2010, 2019; McAdams et al., 2020) and vertebrate animal models (Johnson et al., 2010; Matynia et al., 2012; Delwig et al., 2013; Zhang et al., 2017) are thought to originate from light-evoked signaling in melanopsin-expressing intrinsically photosensitive retinal ganglion cells (ipRGCs). While ipRGCs receive inputs from rods and cones (Güler et al., 2008), they are also photoreceptors themselves: melanopsin phototransduction is sufficient for photoaversion in adult *rd/rd cl* mice (Semo et al., 2010) and required for photoaversion in neonatal mice (Johnson et al., 2010), before the maturation of bipolar cell synapses with retinal ganglion cells on postnatal day 10 (P10) (Hoon et al., 2014).

What is the encoding of a light stimulus that evokes an aversive response? ipRGCs comprise multiple types, denoted M1-M6 in mice (Do, 2019; Aranda and Schmidt, 2021), with M1-M5 present in the neonatal retina (Caval-Holme et al., 2019; Lucas and Schmidt, 2019). M1-M6 differ in their light response properties, the molecules involved in their phototransduction, and the brain areas to which their axons project (Do, 2019; Aranda and Schmidt, 2021). Many of these brain regions are thought to relay light information for photoaversion (Routtenberg et al., 1978;) and the negative effects of light on mood (Fernandez et al., 2018; An et al., 2020). Divergent axonal projections and previous demonstrations of type-specific contributions to non–image-forming functions (Chen et al., 2011; Rupp et al., 2019) raise the possibility that activity in a subset of ipRGC types could signal aversion.

The diversity of light responses across ipRGC types is also apparent during development. Gap junction coupling of M2-M5 ipRGCs leads to functional classes that are distinct from anatomic types (Caval-Holme et al., 2019). Blockade of gap junction coupling or enhancement of coupling via reduced dopamine signaling leads to corresponding changes in the photosensitivity of M2-M5 ipRGCs (Kirkby and Feller, 2013; Arroyo et al., 2016; Caval-Holme et al., 2019). In contrast, M1 photosensitivity is invariant to modulation of gap junction coupling and therefore cell-autonomous (Caval-Holme et al., 2019). It is unknown how these developing circuits involving ipRGCs contribute to photoaversion.

Moreover, during the same developmental stage at which neonatal rodents exhibit photoaversion, the retina generates spontaneous activity patterns called retinal waves (Feller et al., 1996, 1997; Blankenship and Feller, 2010; Wong et al., 2000) that are thought to depolarize all RGCs (Ford et al., 2012), including ipRGCs (Kirkby and Feller, 2013). Excitation from retinal waves propagates along the axons of RGCs into the brain (Mooney et al., 1996; Weliky and Katz, 1999; Ackman et al., 2012) and seems poised to interfere with the detection of light that drives photoaversion. However, neonatal mice exhibit limited physical activity in the dark (Johnson et al., 2010; Delwig et al., 2013), indicating that retinal waves do not trigger a photoaversion-like behavior.

Here, we use a variety of approaches, including transgenic mice and pharmacology, to reveal which ipRGC types mediate photoaversion in neonatal mice. Additionally, we reveal that these ipRGCs exhibit reduced participation in retinal waves. Together, these data indicate that the signals underpinning photoaversion are reliable and informative.

Materials and Methods

Experimental model and subject details

Animal procedures were approved by the University of California Berkeley Institutional Animal Care and Use Committees and conformed to the National Institutes of Health's *Guide for the care and use of laboratory animals*, the Public Health Service Policy, and the Society for Neuroscience Policy on the Use of Animals in Neuroscience Research. Photoaversion assays were performed on P7 and P8 mice of either sex. Animal health was monitored daily, and only healthy animals were used in experiments. WT mice were from the C57BL/6J strain. Melanopsin KO mice were generated by crossing $Opn4^{Cre/+}$ mice, in which one of the copies of melanopsin is replaced by Cre, to generate $Opn4^{Cre/Cre}$ homozygotes. *TrpC 6/7* KO mice were generated from *TrpC 3/6/7* KO mice obtained from Professor Tiffany Schmidt (Northwestern University). As *TrpC* KO mice were generated on a 1:1 C57BL/6J:C129 genetic background, 1:1 C57BL/6J:C129 WT mice served as controls for experiments with *TrpC* 6/7 KOs.

Method details

Photoaversion assay apparatus. The behavior chamber consisted of an open-topped transparent plastic box (Warner Instruments) measuring 10.8 × 3.5 × 2.5 cm (L × W × H). The chamber was painted on all surfaces (except the inner and outer faces at one end, left transparent for light entry) with matte black low-aerosol spray paint. Matte black construction paper was cut into a rectangle and placed on the chamber floor to provide traction and minimize optical reflections that interfered with automated tracking of mice, with a fresh piece of paper used for each behavioral session. The base of the chamber was warmed to 35 ± 2°C by a heating pad, and the temperature was monitored continuously with a thermistor probe (Warner Instruments).

Video monitoring of the behavior was achieved with a camera (Thorlabs CS165MU with Thorcam software) fitted with a high-pass optical filter (Thorlabs FEL0600) to prevent light from the stimulus LED from reaching the detector. The camera, along with an infrared LED light source (Thorlabs M970L4, λ_{max} = 970 nm) fitted with a spherical lens, was mounted on a pole and focused on the chamber from 45 cm above the floor of the chamber. Video frames at a resolution of 32 × 105 pixels were collected at 27.5 frames/s.

The light stimulus was delivered by an LED (Luxeon SP-05-B4 LED module; λ_{max} = 470 nm; FWHM = 15 nm) coupled to collimating optics (Thorlabs). The timing and intensity of light stimulation were controlled with pulse width modulation, using an Arduino Uno running custom software written in the Arduino programming language. The onset of a light stimulus also triggered a brief flash from an infrared LED (LED Supply L3-0-IR5TH50-1, λ_{max} = 850 nm) mounted within the FOV of the camera but out of the line of sight of the mouse, thus recording the timing of the light stimulus within the video of each behavioral trial (the infrared light also flashed during the dark trials). Irradiance measurements were obtained by converting measurements of optical power to photon flux. Measurements of optical power were constant along the length of the chamber, as expected for a minimally diverging light beam.

Photoaversion assay. Mice were dark-adapted in the home cage for 1 h before experiments. During a behavioral session, a mouse pup was removed from the home cage, and an infrared-reflective sticker was affixed to its head. The center of the sticker was centered between the ears with respect to the rostral-caudal body axis. The mouse pup was then acclimated to the chamber for 4 min. Before each trial, the mouse was placed in the chamber with its head angled to within 30° of the stimulus source (the axis of the collimated light beam from the LED); we collimated the LED light after observing in pilot experiments using point-source stimuli (the LED lens only) that the magnitude and dynamics of the turning response varied with the distance of the mouse to the source, as expected for a highly diverging beam.

Video recording commenced and the pup was monitored for 30 s in the dark. If the pup turned so that its head angle exceeded 45° from the LED, it was repositioned, and the trial restarted. A maximum of 3 restarts were allowed before a pup would be excluded from the study. When individual pups were tested on repeated trials that included light stimuli, they were left for 60 s in the dark between trials to allow the ipRGCs to partially recover from light adaptation (Do and Yau, 2013). In pilot experiments, we observed that the magnitude and dynamics of the light-evoked turning behavior were similar for up to three trials at the saturating irradiance (9 log units; data not shown). After a behavioral session, the chamber was cleaned with 70% ethanol, which was allowed to evaporate for 4 min before commencing a session with the next mouse. To minimize differences in the behavior because of circadian variability, we performed experiments only during the subjective day portion of the 12/12 h light/dark cycle in the rodent housing rooms.

Open field test. To measure movement without activating photoaversion pathways, we performed an open field test in which we placed a P11 pup into a room temperature (20°C) Pyrex beaker with an open top. Lighting conditions were dim enough not to evoke a photoaversion response. Behavioral recordings were made using the same camera as in the Photoaversion assay, with a resolution of 381 × 365 pixels at 15 frames/s.

Enucleation. Enucleation procedures were conducted just after birth (P0). A maximum of 1 h of nursing was allowed before surgery. Pups

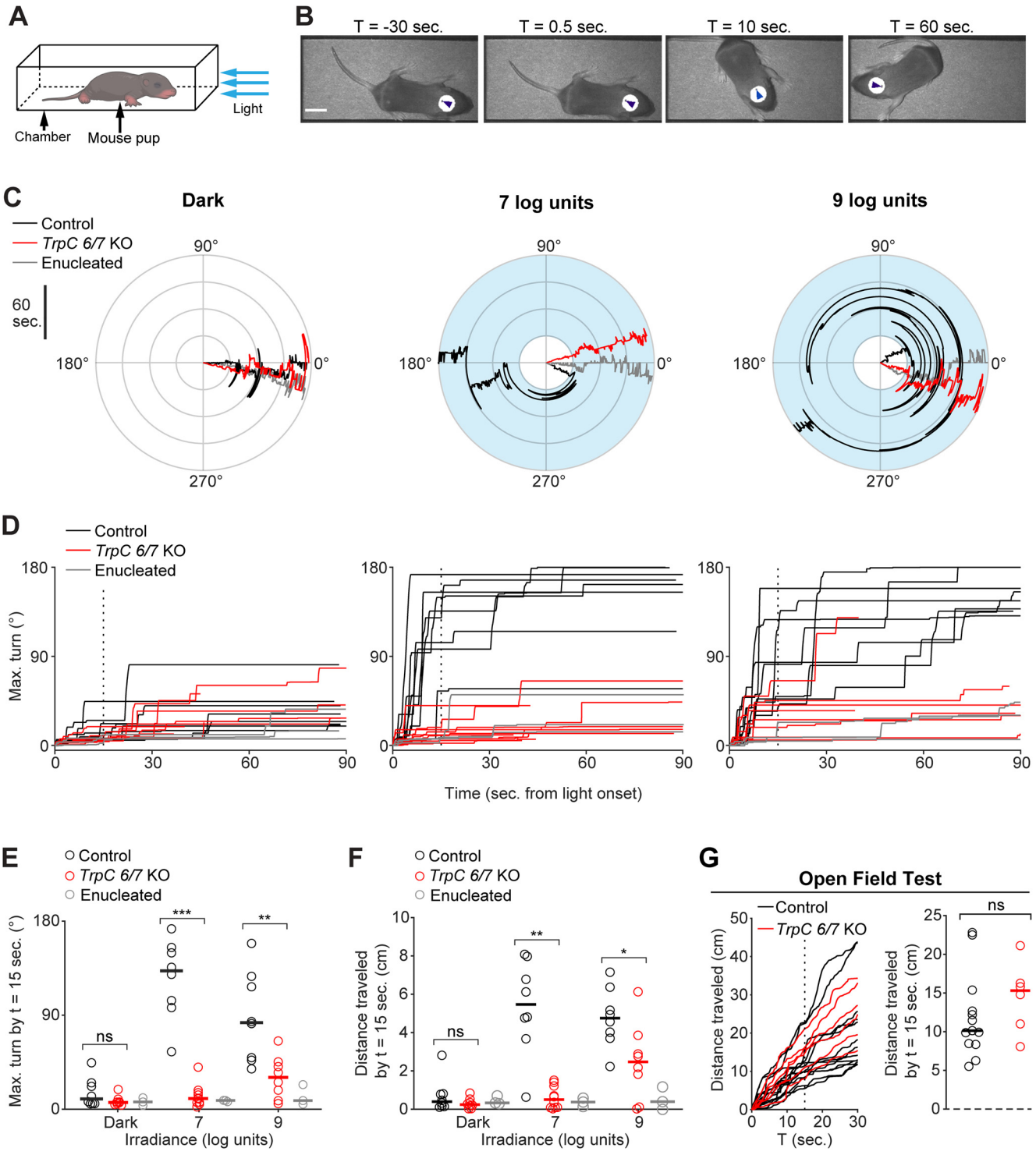

Figure 1. Photoaversion requires *TrpC 6/7*. ***A***, Testing apparatus. Mouse pups (aged P8, unless noted otherwise) were placed in a chamber. Trials began with a 30 s baseline in the dark. If the mouse remained oriented toward the LED (head angle $<45°$), the trial proceeded for an additional 90 s, either in darkness or with a light stimulus (blue arrows; $\lambda_{max} = 470$ nm; FWHM = 29 nm). Pups were monitored from above with infrared illumination ($\lambda_{max} = 970$ nm) to which melanopsin is $\sim 10^{12}$-fold less sensitive (Emanuel and Do, 2015) (for further details, see Materials and Methods). ***B***, Video frames depicting the avoidance response of a C57BL6/J mouse pup to a light stimulus (10^7 photons μm^{-2} s^{-1}; onset at $t = 0$ s). Arrowheads indicate automated tracking. Scale bar, 1 cm. ***C***, Polar plots of head angle during representative behavioral tests of Control (black traces), *TrpC 6/7* KO (red traces), and enucleated (gray traces; bilaterally at P0; see Materials and Methods) mice in darkness (left) or with exposure to two different light intensities (middle and right; 7 log units = 10^7 photons μm^{-2} s^{-1}). Blue shading represents the timing of the light stimulus. Time emanates outwards. ***D***, Head turns of genetic background control mice (Control, 1:1 C129:C57BL6/J; black traces), mice lacking TRPC6 and TRPC7 ion channels (*TrpC 6/7* KO; red traces), and enucleated mice (gray traces) as a function of light intensity. Vertical dashed line: time sample (15 s) used for statistical comparisons in ***E*** and ***F***. Each mouse was tested in darkness and at both light intensities. $N = 8$ Control and *TrpC 6/7* KO mice and 3 enucleated mice. Enucleated mice in light (7 log units) versus darkness: $p > 0.99$. Sham-operated control versus enucleated mice: $p < 0.0001$. $N = 3$ mice per group. Two-way ANOVA with Tukey-Kramer *post hoc* test. ***E***, Comparison of head turns of Control, *TrpC 6/7* KO, and enucleated mice, sampled 15 s after light onset. Error bars indicate medians. Not significant ($p = 0.19$). $^{**}p < 0.005$; $^{***}p < 0.0005$; Wilcoxon rank-sum test. Same mice as in ***D***. ***F***, Comparison of movement (travel distance of the centroid of the infrared-reflective sticker) of Control, *TrpC 6/7* KO, and enucleated mice sampled 15 s after light onset. Error bars indicate medians. Not significant ($p = 0.51$). $^{*}p < 0.05$; $^{**}p < 0.005$; Wilcoxon rank-sum test. Some trials were excluded because of head-tracking errors. Same mice as in ***D*** and ***E***. ***G***, An open field test indicated no difference

were anesthetized with an intraperitoneal injection of a mixture of ketamine (40 mg/kg) and xylazine (5 mg/kg), then placed on ice for 1-4 min. A toe-pinch was performed to confirm the appropriate level of surgical anesthesia, after which the eyelid was cleaned using aseptic technique.

An incision was first made in each eyelid with a scalpel. The eye was lifted away from the orbit with forceps and severed from the optic nerve with surgical scissors. The eyelid was sealed with 0.5 μl to 1 μl of tissue adhesive (Surgi-Lock instant liquid tissue adhesive, Fisher Scientific). The procedure was then replicated on the other eye. Sham surgeries omitted the enucleation step but were otherwise identical.

After enucleation, the pups were immersed in lukewarm water bath for 30 s followed by an application of lidocaine hydrochloride jelly USP, 2% (Akorn) and erythromycin ophthalmic ointment USP, 0.5% (Bausch & Lomb) to prevent pain, swelling, and infection. At the end of the procedure, buprenorphine was administered and repeated 6-8 h later. Pups were then evaluated the following day for additional need. In addition, an NSAID (meloxicam) was given at the end of the procedure and repeated the following day. Pups were housed with their mother in a cage with nesting material before and after surgery. At P8, the pups were tested in the photoaversion assay.

Intraocular injections. Intraocular injections were performed as described previously. Drugs were dissolved in PBS and injected at concentrations of 500 μM (meclofenamic acid [MFA]) and 100 μM (SCH23390). Injections delivered 0.5 µl of solution into the vitreous cavity, which at P7-8 contains a volume of ~3.5 μl (Kaplan et al., 2010). The concentrations of the drugs in the vitreous cavity would thus be reduced by a factor of ~0.14, to ~71 μM MFA and 14 μM SCH. Mice were recovered and dark adapted for $\geq$1 h after injections.

Ex vivo *retina preparation.* Mice were deeply anesthetized with isoflurane inhalation and killed by decapitation. Eyes were immediately enucleated, and retinas were dissected in oxygenated (95% O_2, 5% CO_2) ACSF (in mM as follows: 119 NaCl, 2.5 KCl, 1.3 $MgCl_2$, 1 K_2HPO_4, 26.2 $NaHCO_3$, 11 D-glucose, and 2.5 $CaCl_2$) at room temperature under white light. In some experiments, 0.1 μM sulforhodamine 101 (SR101, Invitrogen) was added for visualization of vasculature. Each isolated retina was cut into two pieces. Each piece of retina was mounted over a 1-2 mm^2 hole in nitrocellulose filter paper (Millipore) with the photoreceptor layer side down, dark-adapted for 1 h, and transferred to the recording chamber of a two-photon microscope for imaging or electrophysiological recording. The whole-mount retinas were continuously perfused (3 ml/min) with oxygenated ACSF warmed to 32°-34°C by a regulated inline heater (TC-344B, Warner Instruments) for the duration of the experiment. Additional retina pieces were kept in the dark at room temperature in ACSF bubbled with 95% O_2, 5% CO_2 until use (maximum 8 h).

Ex vivo *visual stimulation.* Visual stimuli were delivered by LEDs (Thorlabs M420L2 or M470L2 λ_{max} = 420 or 470 nm; FWHM = 15 nm) coupled to a digital micromirror device (Digital Light Innovations Cel 5500). Stimuli were regularly calibrated with a radiometer (Newport). The intensity of the stimulus ranged from 10^4 to 10^8 photons μm^{-2} s^{-1}, replicating the range of light intensities present at the retina from twilight to full sunlight (Allen et al., 2014). Each light stimulus lasted 30 s and was separated from the previous light stimulus by 60 s. The stimuli had a 100% positive contrast (bright on dark background).

To decrease the background signal during the stimulus (because of emission by the phosphorescent objective glass and Cal 590, following absorption of the stimulus light), the stimulus was interleaved with imaging. The stimulus was delivered on the flyback of the fast axis scanning mirror during a unidirectional scan.

Two-photon calcium imaging. Each retina was cut into halves. To maintain control over light history, only one field of view (FOV) was sampled from each half. Retina halves were bulk-loaded with the calcium indicator Cal 590 A.M. (AAT Bioquest) using a multicell bolus loading technique described previously (Stosiek et al., 2003; Blankenship et al., 2009). Two-photon fluorescence measurements were obtained with a modified movable objective microscope (Sutter instruments) using an Olympus 60×, 1.00 NA, LUMPlanFLN objective (Olympus America) for single-cell resolution imaging (FOV: 203 - × 203 µm). This movable objective microscope was equipped with through-the-objective light stimulation and two detection channels for fluorescence imaging. Two-photon excitation was evoked with an ultrafast pulsed laser (Chameleon Ultra II; Coherent) tuned to 1040 nm to image Cal 590 A.M. Di-hydro-β-erythroidine (DHβE, 8 μM, Tocris Bioscience) was added to the perfusion system immediately before imaging to block spontaneous retinal waves that would otherwise interfere with measurements of light responses. Previously, we showed that extended ($\geq$1 h) blockade of waves with DHβE leads to an increase in the number of light-sensitive cells (Arroyo et al., 2016). We conducted all experiments within the first 20 min of wave blockade, during which time the number of light-responsive cells does not increase (Caval-Holme et al., 2019). Laser power was set to 6.5 µW for imaging Cal 590 A.M. The microscope system was controlled by ScanImage software (www.scanimage.org). Scan parameters were [pixels/line × lines/frame (frame rate in Hz)]: [256 × 256 (1.48 Hz)], at 2 ms/line.

Immunoassays. Whole-mount retinas were removed from the recording chamber and transferred to a 4% PFA solution for 20 min at room temperature. Following fixation, retinas were washed in blocking buffer (1.5% BSA, 0.2% Na-Azide, 0.2% Triton X-100; 3 times, 10 min each time). Retinas were then incubated in a primary immunoreaction solution for 1-3 d at 4°C. Primary immunoreaction solution consisted of blocking buffer that contained 1:1000 rabbit anti-melanopsin (ATS Bio AB N38) and 1:250 mouse anti-SMI32 (Biolegend 801701). After incubation in the primary immunoreaction solution, retinas were washed in PBS (3 times, 10 min each time), and then incubated for 2 h at room temperature in secondary immunoreactive solution containing one or more of the following secondary antibodies: 1:1000 donkey anti-rabbit conjugated to Alexa-488 (Invitrogen A21206) and 1:1000 goat anti-mouse conjugated to Alexa-647 (Invitrogen A21235). Retinas were washed again in PBS and then mounted on slides with an anti-fade agent (Vectashield H-1400, Vector Laboratories).

Experimental design and statistical analysis

Tracking of mouse head angle and position. After photoaversion assays, we tracked mouse head angle and position via automated tracking of a circular infrared-reflective sticker affixed to pups' heads 'circular fiducial', using a custom algorithm implemented as a plugin in ImageJ (neonates also produce ultrasonic vocalizations in response to bright light (Delwig et al., 2012). However, we found this to be more variable than movement). The fiducial was fabricated from a roll of infrared-reflective tape using a hole punch. Specifically, the circular fiducial was tracked in each movie frame using a Hough circle transform (HCT). While the HCT is very robust as segmenting circular objects in an image, it also adds an extra dimension to the search space corresponding to the circle radius and therefore is computationally intensive. We developed a modified HCT to track the circular fiducial with less computational time. After the circular fiducial is found in the first frame of the movie, the transform and search space in the following frames are narrowed down to a fiducial of similar radius and position. The algorithm was additionally optimized by multiprocessing both the transform and search algorithms. More details on the HCT plugin can be found here: https://imagej.net/Hough_Circle_Transform.

To measure head orientation, a black dot was added to the inside edge of the circular fiducial. This allowed for extraction of orientation as a vector from the center of the black dot to the center of the circular fiducial. An ImageJ macro was written that used the HCT plugin to find the circular fiducial and segmented the black dot with the circle to obtain the vector orientation. The ImageJ macro used can be found here:

←

between locomotion in Control (black traces) and *TrpC 6/7* KO (red traces) mouse pups tested at P11. Left, Travel distance during the open field test. Vertical dashed line indicates the time sample (15 s) used for statistical comparison. Right, Comparison of locomotion. Error bars indicate medians. $p = 0.28$ (Wilcoxon rank-sum test). $N = 13$ Control mice and 6 *TrpC 6/7* KO mice.

https://github.com/Llamero/Mouse_tracking_macro. To quantify pups' movements in the open field test, we tracked the base of the tail using deepLabCut (Nath et al., 2019).

Behavioral quantification. We wrote custom algorithms in MATLAB to preprocess and analyze the raw head angle and position data from the HCT tracking program and deepLabCut. Mouse head angle and position were filtered, to interpolate over brief (<1 s.) tracking errors. Turn angles were defined as the angular difference between the head angle at each time-sample and the mean head angle within the 0.5 s before stimulus onset.

Image analysis of population calcium imaging movies. Movies were spatially median-filtered to remove high-frequency noise and then registered relative to a frame in the middle of the movie to remove mechanical drift. The baseline movie frame (F_0) was computed by taking the temporal median projection of all the movie frames. Each movie frame F was normalized by dividing its difference from the baseline frame ($F - F_0$) by the baseline frame ($(F - F_0)/F_0$) to produce a $\Delta F/F_0$ movie. Circular ROIs were drawn on cells that displayed >20% increases in $\Delta F/F_0$ during at least one of the light stimuli. The ROIs and the $\Delta F/F_0$ movie were then imported into MATLAB for further analysis using custom algorithms. Traces for each ROI were computed as the mean value of the pixels enclosed by the ROI in each frame of the $\Delta F/F_0$ movie. For each ROI, the amplitude of the response to each light stimulus was computed as the difference between the peak $\Delta F/F_0$ value during the light stimulus and the $\Delta F/F_0$ value during the movie frame before the light stimulus. ROIs were defined as "light-responsive" if the maximum amplitude of their $\Delta F/F_0$ signal during any light stimulus exceeded the mean $\Delta F/F_0$ in the 30 s interval preceding the light stimulus by more than 6 SDs.

Unsupervised clustering of light-evoked fluorescence transients. Fluorescence traces for all light-responsive cells were combined into a single matrix (cells × movie frames). The traces were high pass filtered at 0.01 Hz to remove slow changes in fluorescence caused by mechanical drift in the *z* axis and the samples corresponding to the 30 s preceding each light stimulus were removed. Each trace was normalized to its own maximum value. Functional clustering of light-responsive cells from genetic background control mice was performed as described previously (Baden et al., 2016; Caval-Holme et al., 2019) and culminated in a set of sparse principal components weights and a Gaussian mixture model. To classify light-responsive cells from TRPC 6/7 KO mice, we used the sPCA weights computed from the genetic background dataset to project their fluorescence traces onto the principal components. We then used the GMM from the genetic background dataset to assign the TRPC 6/7 KO cells to functional clusters.

Identification of ipRGC types. ipRGC types were identified at the conclusion of two-photon calcium imaging sessions using one of two strategies. In Opn4::eGFP mice, *z* stacks of GFP^+ cells in the live retina were collected. In other mouse lines, ipRGCs were identified using melanopsin immunostaining. In the latter approach, FOV in the fixed tissue were realigned to FOV from two-photon calcium imaging by registration of common landmarks in the vasculature. Vasculature was visualized in live tissue using SR101 and in fixed tissue using an antibody against the neurofilament protein SMI32 that fortuitously labels blood vessels (see Immunoassays). In both approaches, M1 ipRGCs were identified by their dendritic stratification at the outermost boundary of the inner plexiform layer, close to the inner nuclear layer (Caval-Holme et al., 2019).

Analysis of retinal waves. Interwave interval population wave frames were identified by finding peak ΔF/F transients in the average trace of the whole FOV, using the MATLAB findpeaks functions with a minimum peak prominence of 1.5 after *z* scoring. The difference between consecutive population wave locations was taken to be the interwave interval. Wave-triggered average ΔF/F traces, each spanning 11 frames, centered around population wave peaks for the whole FOV, were averaged for each neuron to produce the wave-triggered average. A bootstrapping approach was used to generate a null distribution of randomly triggered averages. For each neuron with a given number of wave locations, the same number of virtual population wave locations were generated, such that the 11-frame window around the virtual wave location would not overlap with any of the actual wave windows. Averages were computed with the virtual locations in an otherwise identical manner and were computed with a new set of virtual wave locations 1000 times per neuron. A 95th percentile array was computed with the MATLAB prctile function applied to this array of 1000 averaged traces. A neuron with a wave-triggered average that at any point exceeded this 95th percentile array was defined as participating in retinal waves and was otherwise defined as exempt from the retinal wave.

Statistical analyses

Data that significantly violated the assumptions of parametric statistical tests were assessed using nonparametric tests. Wilcoxon-rank sum tests were used to compare medians of independent samples. Error bars indicate bootstrapped 95% CIs. Horizontal bars represent medians. The number of replicates and statistical results are provided in the figure legends.

Materials availability

This study did not generate new unique reagents.

Code accessibility

The photoaversion behavior and two-photon calcium imaging datasets have been deposited, in a preprocessed format, at Mendeley (DOI: 10.17632/mwxrm8g5jz.1) and are publicly available as of the date of publication. Electrophysiology and immunohistochemistry datasets are available upon request. All original code has been deposited at https://github.com/FellerLabCodeShare and https://github.com/Llamero/Mouse_tracking_macro and is publicly available as of the date of publication.

Results

Intensity threshold for photoaversion consistent with M1 or M3 photosensitivity

We first compared the light intensity threshold for photoaversion with the light intensity thresholds for the different types of ipRGCs, which vary over ~2 orders of magnitude (Tu et al., 2005; Caval-Holme et al., 2019; Lucas and Schmidt, 2019). To determine the light intensity threshold for photoaversion, we recorded movies of freely moving postnatal day 8 (P8) mice within a rectangular chamber, in darkness or with a beam of monochromatic blue light (λ_{max} = 470 nm; FWHM = 29 nm; see Materials and Methods) entering from one end (Fig. 1*A*). We used automated tracking to measure head angle, as the maximum angle of deflection of the head away from the light source over time, and position within the chamber. The light was considered aversive if mice turned their heads and moved away from the light source (Fig. 1*B*) (Johnson et al., 2010; Delwig et al., 2013; Jones et al., 2013; Mure et al., 2018). Photoaversion was absent in bilaterally enucleated mice (Fig. 1*C*), consistent with a study in neonatal rats (Routtenberg et al., 1978), ruling out a role for melanopsin expression outside the eye (Sikka et al., 2014; Matynia et al., 2016; Delwig et al., 2018). Neonatal mice exhibited photoaversion at light intensities > 10^7 photons μm^{-2} s^{-1} (Fig. 1*D*), corresponding to ~10^5 photons μm^{-2} s^{-1} at the retina, assuming a 100-fold loss of intensity from the outside of the closed eyelids (Tiriac et al., 2018) to the retina. Ca^{2+} imaging and electrophysiology experiments in *ex vivo* retinas indicate that this light intensity reliably depolarizes neonatal M1s and M3s (Tu et al., 2005; Schmidt et al., 2008), but not M2s, M4s, and M5s (Caval-Holme et al., 2019).

Photoaversion requires *TrpC 6/7*

To identify the type of ipRGCs that mediate photoaversion, we first sought to identify the phototransduction mechanisms involved in the behavior. To this end, we measured the behavior

in mice that lack TRPC6 and TRPC7 ion channels (*TrpC 6/7* KO), the primary phototransduction channels in M1 ipRGCs (Xue et al., 2011; Jiang et al., 2018; Sonoda et al., 2018). Strikingly, P8 *TrpC 6/7* KO mice had no detectable response to the threshold intensity for WT mice (10^7 photons μm^{-2} s^{-1}; Fig. 1*D*,*E*). In response to a saturating intensity (10^9 photons μm^{-2} s^{-1}), *TrpC 6/7* KO mice made small head turns and movements (Fig. 1*E*,*F*; 2 of 8 *TrpC 6/7* KO mice turned >45° within 90 s of light onset, compared with 8 of 8 genetic background control mice; for videos of the behavior, see http://fellerlab.squarespace.com/movies). Dramatically reduced photoaversion in *TrpC 6/7* KO mice did not result from a general movement deficit, as *TrpC 6/7* KO and control mice traveled similar distances during an open field test (Fig. 1*G*; see Materials and Methods). TRPC6/7 ion channels are therefore critical for photoaversion, with remaining phototransduction mechanisms enabling residual behavioral responses to a saturating light intensity.

M1 ipRGCs of *TrpC 6/7* KO mice exhibit reduced photosensitivity

In adult *TrpC 6/7* KO mice, M1s lack virtually all photocurrent (Xue et al., 2011), M2s lack a portion of their photocurrent (Jiang et al., 2018; Perez-Leighton et al., 2011), and M4s are unaffected (Jiang et al., 2018; Sonoda et al., 2018). A transcriptomic study indicates that M1s are the only RGC type with high levels of *TrpC 6/7* expression (Tran et al., 2019). Photocurrents and other physiological properties of M1 and M2 ipRGCs in early postnatal mice resemble those in adult mice (Lucas and Schmidt, 2019), but conductances in *TrpC 6/7* KOs at these early ages were not directly compared. The functional role of TRPC6/7 in developing ipRGCs is therefore unknown. To characterize the neonatal retina's population light response in the absence of TRPC6/7 phototransduction, we used two-photon Ca^{2+} imaging to measure light-evoked responses from individual neurons within the ganglion cell layers of retinas from P7-P9 WT and *TrpC 6/7* KO mice. We presented a range of light intensities (10^4 to 10^8 photons μm^{-2} s^{-1}; 420 or 470 nm; see Materials and Methods) (Fig. 2*A*) corresponding to ~10^6 to 10^{10} photons μm^{-2} s^{-1} *in vivo* during the photoaversion assay. To isolate light-evoked Ca^{2+} transients from those triggered by retinal waves, we superfused retinas with a solution containing the nicotinic acetylcholine antagonist Dihydro-β-erythroidine hydrobromide (DHβE) (8 μM) (Bansal et al., 2000). The retinas of *TrpC 6/7* KO mice contained light-responsive cells, but these were present at a lower density (Fig. 2*B*), consistent with a subset of ipRGCs dependent on TRPC6/7 for phototransduction.

To determine which ipRGC types have disrupted photosensitivity in *TrpC 6/7* KO retinas, we first computationally classified cells according to their light-evoked Ca^{2+} transients (Fig. 2*C*,*D*) (Baden et al., 2016; Caval-Holme et al., 2019). We identified four functional types of cells in the WT retinas, defined by the threshold and duration of their light responses: high sensitivity (HS), moderate sensitivity (MS), low sensitivity transient (LST), and low sensitivity sustained (LSS). We then used the model that identified functional types in the WT to classify light-responsive cells in the *TrpC 6/7* KO retinas (see Materials and Methods). Notably, *TrpC 6/7* KO retinas contained cells of each functional type found in the WT, though with a lower density of HS cells (Fig. 2*E*). Moreover, compared with HS cells in the WT, the HS cells in the *TrpC 6/7* KO had similar light-intensity thresholds but smaller amplitude Ca^{2+} transients (Fig. 2*F*). Irradiance tuning of Ca^{2+} transients in other functional types (MS, LST, and LSS) was unaffected. Hence, we hypothesize that the reduced light sensitivity of the population of HS cells in the *TrpC 6/7* KO is insufficient to drive photoaversion at these lower light intensities.

The light-evoked Ca^{2+} transients of HS cells closely resembled those previously reported for neonatal M1s (Caval-Holme et al., 2019). To determine whether HS cells corresponded to M1s, we anatomically identified M1s after Ca^{2+} imaging by imaging their dendrites (which stratify exclusively in the OFF sublamina of the inner plexiform layer), either in postfixed retinas, using melanopsin immunohistochemistry (data not shown), or in the living *ex vivo* retinas of mice that express GFP under the control of the *Opn4* gene (Opn4::eGFP) (Schmidt et al., 2008; Caval-Holme et al., 2019). Our unsupervised classification closely reflected the anatomy: 6 of 7 of the anatomically identified M1s were assigned to the HS functional type, with the remaining M1 assigned to the MS functional type. Thus, reduced photoaversion in *TrpC 6/7* KO mice corresponded with a specific reduction in M1 photosensitivity. These results are consistent with a recent transcriptomics study that shows high expression of *TrpC* 6/7 in M1s and undetectable levels in M2s during early postnatal development (Shekhar et al., 2022).

Normal photoaversion in mice with only M1 ipRGCs

To determine whether signaling from M1 ipRGCs alone is sufficient for photoaversion, we measured the behavior in $Opn4^{Cre}$ $Brn3b^{DTA}$ mice (DTA), in which Cre-dependent expression of diphtheria toxin under the control of the *Brn3b* promoter ablates all ipRGCs by P7, except a subset of ~400 M1s that lack *Brn3b* expression (Chen et al., 2011; Chew et al., 2017). Remarkably, DTA mice exhibited photoaversion indistinguishable from littermate controls (Fig. 3), despite their lack of M2-M6 ipRGCs. Thus, signals originating from a subset of M1 ipRGCs are enough to drive photoaversion over a hundred-fold range of light intensity.

Photoaversion does not require gap junction coupling in the retina

Our previous studies indicate that non-M1 ipRGCs are extensively gap junction coupled and that blockade of gap junction coupling significantly diminishes the photosensitivity of M2-M6, but not M1s (Caval-Holme et al., 2019) (Fig. 4*A*). Hence, to investigate whether signaling from the non-M1 ipRGCs contributes to photoaversion, we assayed photoaversion in mice that received intraocular injections of the gap junction antagonist meclofenamic acid (MFA; ~70 μM in the vitreous). Mice injected with MFA exhibited photoaversion behavior indistinguishable from saline-injected littermate controls (Fig. 4*B*,*C*), suggesting that disruption of photosensitivity in M2-M6, but not M1, had little effect on photoaversion.

We also performed bilateral intraocular injections of the Type 1 dopamine receptor antagonist SCH23390 (~14 μM in the vitreous humor). This manipulation increases light sensitivity, primarily in M2-M6 ipRGCs, via an increase in gap junction coupling (Caval-Holme et al., 2019). Mice injected with SCH23390 exhibited similar photoaversion to saline-injected littermate controls (Fig. 4*D*,*E*). If M2-M6 contribute to photoaversion at lower light intensities, we hypothesized that mice injected with SCH23390 would respond to a 10^6 photon μm^{-2} s^{-1} light stimulus (below the light intensity threshold for photoaversion in WT mice).

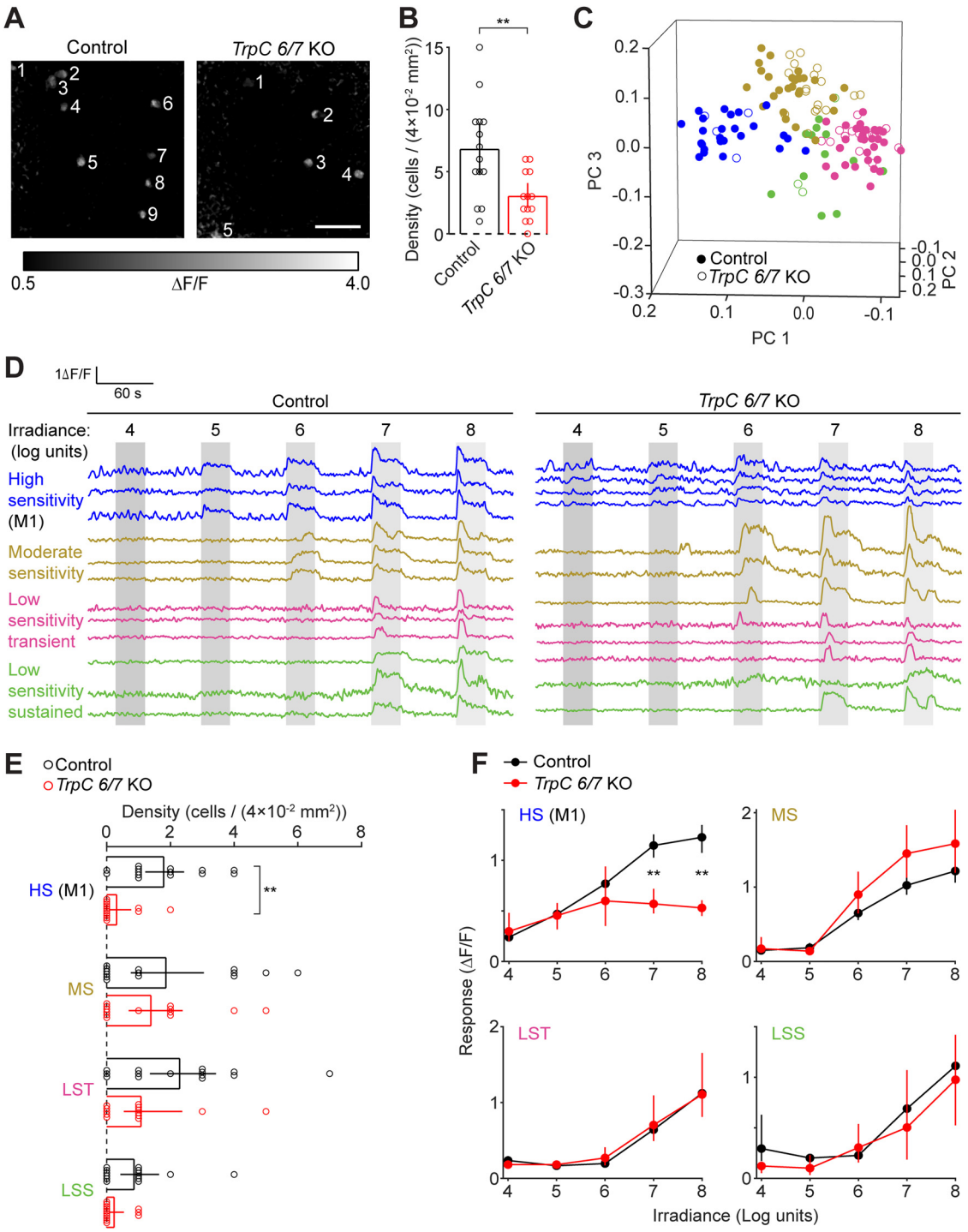

Figure 2. M1 ipRGCs of *TrpC 6/7* KO mice exhibit reduced photosensitivity. ***A***, Fluorescence responses to the presentation of a light stimulus (λ_{max} = 470 nm, 10^8 photons μm^{-2} s^{-1}) observed with two-photon imaging of the Ca^{2+} indicator Cal 590 A.M. Representative FOV (200 × 200 μm) are depicted for a retina from a WT control mouse (left, from a matched genetic background [1:1 C129:C57BL6/J]; and right, a *TrpC 6/7* KO mouse). Numbering indicates light-sensitive cells. Scale bar, 50 μm. ***B***, Comparison of the number of light-sensitive cells per FOV. Error bars indicate bootstrapped 95% CIs. $^{**}p < 0.005$ (two-sample *t* test). Control: $n = 14$ FOV from 5 mice. *TrpC 6/7* KO: $n = 13$ FOV from 4 mice. ***C***, Visualization of each cell's light-evoked fluorescence transient within the space of the first three principal components of population activity. Each point represents a cell from the retina of a Control (closed symbols) or *TrpC 6/7* KO mouse (open symbols). Point colors represent functional clusters named in ***D***. ***D***, Fluorescence traces (ΔF/F) from representative cells of each functional cluster recorded in the retinas of Control (left) and *TrpC 6/7* KO (right) mice. Functional clusters are named and color-coded according to the sensitivity (irradiance threshold) and duration of their light responses. Gray bars represent the timing of light stimuli: 4-8 log units: 10^4-10^8 photons μm^{-2} s^{-1}. ***E***, Comparison of the number of cells within each functional cluster, per FOV, in Control and *TrpC 6/7* KO retinas. $^{**}p < 0.005$. Not significant ($p > 0.05$). Wilcoxon signed-rank test. ***F***, Comparison of irradiance-response relations between control and *TrpC 6/7* KO cells within each functional cluster. $^{**}p < 0.005$ (Wilcoxon signed-rank test). Control: $n = 95$ cells (with 24, 30, 29, and 12 cells assigned to HS, MS, LST, and LSS, respectively). *TrpC 6/7* KO: $n = 39$ cells (with 4, 14, 19, and 2 cells assigned to HS, MS, LST, and LSS, respectively). Same cells as in ***E***.

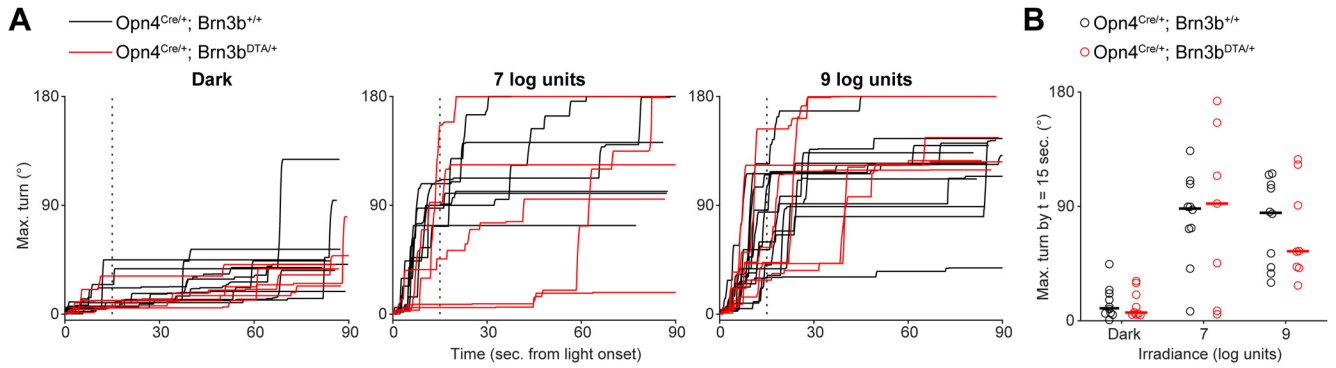

Figure 3. Normal photoaversion in mice with only M1 ipRGCs. ***A***, Head turns in littermate Opn4^{Cre} mice (Control; black traces) and Opn4^{Cre} *Brn3b*^{DTA} mice with diphtheria toxin ablation of all ipRGCs save for ~400 M1s (DTA; red traces): 7 or 9 log units: 10^7 or 10^9 photons μm^{-2} s^{-1}. Each mouse was tested in darkness and at both light intensities. ***B***, Comparison of turns by Control and DTA mice, sampled 15 s after light onset (vertical dashed line in ***A***). Horizontal bars indicate medians. There were no significant differences between turns by Control and DTA mice ($p = 0.78$, 0.74, and 0.97 for Dark, 7 log units, and 9 units, respectively. Wilcoxon rank sum test). $n = 10$ Control and 8 DTA mice. Some mice were excluded from plots in ***A*** because of errors in automated tracking.

However, mice that received SCH23390 did not display an avoidance response to this light intensity (Fig. 4*E*).

Connexin expression, role in ipRGC photosensitivity, and contribution to photoaversion

To complement our pharmacological approach, we used mice that lack specific connexin proteins to assess the impact of disrupted gap junction coupling among ipRGCs on photoaversion. In adults, ipRGCs express Cx30.2 (Meyer et al., 2016) and Cx36 (Harrison et al., 2021). To identify the connexins expressed in ipRGCs in development, we performed immunohistochemical analyses of retinas of mice from three transgenic lines in which regulatory elements of the Cx30.2 (*Cx30.2*$^{lacZ/+}$) (Kreuzberg et al., 2006), Cx36 (*Cx36*$^{lacZ/+}$) (Deans et al., 2001), and Cx45 (*Cx45*$^{fl/+}$) (Maxeiner et al., 2005) genes drive expression of a reporter in place of the endogenous coding sequence (Fig. 5*A*; see Materials and Methods). We crossed the Cx30.2 and Cx36 mutant mice with Opn4::eGFP mice and looked for colocalization of β-galactosidase and GFP. We found that roughly half of GFP$^+$ ipRGCs in the retinas of Cx30.2$^{lacZ/+}$; Opn4::eGFP mice expressed β-galactosidase (Fig. 5*B*,*C*). In Cx36$^{lacZ/+}$; Opn4::eGFP retinas, β-galactosidase expression was sparse in the ganglion cell layer as reported previously (Hansen et al., 2005) and rarely colocalized with GFP$^+$ ipRGCs. β-Galactosidase was expressed in numerous cells within the inner nuclear layer, presumably in AII amacrine cells, indicating that this reaction product accurately reflects Cx36 expression at this age (data not shown).

A third connexin, Cx45, has been observed in RGC types, though not previously associated with ipRGCs (Hansen et al., 2005; Blankenship et al., 2011). To assess the expression of Cx45 in ipRGCs in the neonatal retina, we used an intersectional transgenic strategy in which we crossed Opn4^{Cre} mice with a mouse line in which Cx45 regulatory elements drive expression of eGFP in place of the Cx45 open reading frame (Maxeiner et al., 2005). Thus, in Opn4$^{Cre/+}$ Cx45$^{fl/+}$ retinas, ipRGCs will express both GFP and Cx45 (Fig. 5*A*). Together, these data indicate that neonatal ipRGCs express primarily Cx45, to a lesser extent, Cx30.2, and very little Cx36.

We next assessed the effect of Cx30.2 and Cx45 deletion on the light responses of ipRGCs. In Cx30.2$^{lacZ/lacZ}$ (Cx30.2 KO) and Opn4$^{Cre/+}$ Cx45 $^{fl/fl}$ retinas (in which GFP is present but Cx45 is knocked out; Cx45 KO) retinas, two-photon calcium imaging revealed light-responsive cells at densities that were not significantly different from genetic controls (Fig. 5*D*), suggesting that gap junction circuits are at least partially retained in both KO transgenic lines. As M4 ipRGCs almost universally expressed Cx45 (Fig. 5*C*), we assessed the impact of Cx45 on gap-junction-mediated light responses of M4 ipRGCs. Voltage-clamp recordings of light-evoked currents in M4 ipRGCs from Cx45 KO retinas revealed a significant reduction in the number and amplitude of spikelets (Fig. 5*E*–*I*) but not their elimination (Arroyo et al., 2016; Caval-Holme et al., 2019). Unfortunately, we could not generate a Cx30.2/45 double KO with breeding because these two genes are located on the same chromosome with an estimated recombination frequency of <4%.

Finally, we assessed photoaversion behavior in Cx30.2 KO and Cx45 KO mice (Fig. 5*J*–*M*). At threshold levels of light, Cx30.2 KO and Cx45 KO mice had photoaversion behavior similar to their heterozygous littermates. Cx45 KO mice exhibited a small but statistically significant decrease in light-evoked movement at saturating light levels (Fig. 5*J*,*K*), indicating that gap junction networks may contribute within this saturating stimulation regimen. Because M1 ipRGCs exhibit minimal gap junction coupling in the neonatal retina (Caval-Holme et al., 2019), these results are consistent with M1 ipRGCs providing the principal drive for photoaversion.

M1 ipRGCs are weakly depolarized by retinal waves

At the same age that there is photoaversion, the retina also exhibits retinal waves (Fig. 6*A*) (Feller et al., 1996, 1997; Blankenship and Feller, 2010). These retinal waves are mediated by the diffuse release of excitatory neurotransmitters and are therefore thought to depolarize most cells in the ganglion cell layer, including all RGCs (Ford et al., 2012), including ipRGCs (Kirkby and Feller, 2013). Action potentials generated by retinal waves have been detected in the superior colliculus, lateral geniculate nucleus, and visual cortex (Mooney et al., 1996; Weliky and Katz, 1999; Ackman et al., 2012). However, neonatal mice move little in the absence of light stimuli (Johnson et al., 2010; Delwig et al., 2013), indicating that the motor movements associated with photoaversion are selectively triggered by light-evoked neural activity. How does the neonatal mouse brain distinguish light-induced bursts of action potentials in ipRGCs from those induced by retinal waves?

To test whether the ipRGCs driving photoaversion are strongly activated by retinal waves, we used two-photon Ca^{2+} imaging. We compared the Ca^{2+} transients under three conditions: (1) waves without light responses (Fig. 6*A*); (2) waves with light responses (Fig. 6*B*); and (3) light responses without waves (Fig. 6*C*). Each cell's participation in retinal waves was computed from a retinal wave-triggered average (Fig. 6*D*,*E*). Cells whose

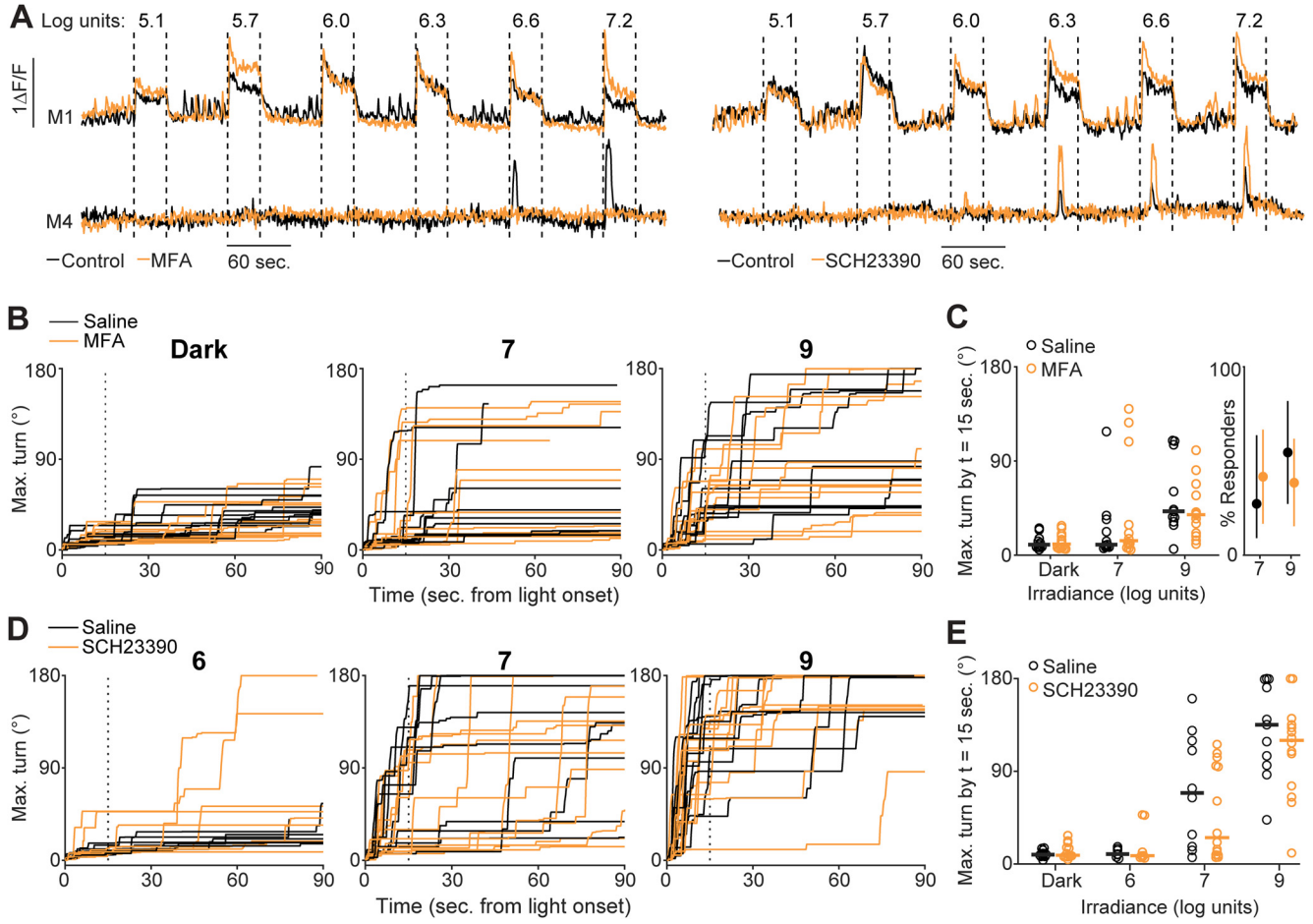

Figure 4. Photoaversion does not require gap junction coupling in the retina. ***A***, Ca^{2+} responses of M1 and M4 ipRGCs in the *ex vivo* retina to a range of light stimulus intensities (e.g., 7.2 log units = $10^{7.2}$ photons μm^{-2} s^{-1}) before (black traces) and after (orange traces) incubation in MFA (a gap junction antagonist; left) or SCH23390 (a Type 1 dopamine receptor antagonist that increases the extent of gap junction coupling; right). Data are replotted from Caval-Holme et al. (2019). ***B***, Time series of maximum head turns of P7 mice that received a bilateral intraocular injection of either saline (black traces) or MFA (orange traces). Panels correspond to trials in darkness (left), trials with a 7 log unit stimulus, or trials with a 9 log unit light stimulus. Vertical dashed line indicates time samples (15 s after light onset) used for quantification in ***C***. Some trials are not displayed because of head-tracking errors. ***C***, Comparison of head turns between the saline and MFA-injected mice in ***B***. Left, Maximum turn angle 15 s after stimulus onset. Horizontal lines indicate medians. Wilcoxon rank-sum test: $p = 1.00$, 0.73, and 0.60 for dark, 7 log unit, and 9 log unit trials, respectively. $n = 11$ saline-injected mice and 13 MFA-injected mice. Right, Proportion of mice that responded to light with large head turns (a turn >90° within 90 s of stimulus onset). Points represent mean response rate. Error bars indicate bootstrapped 95% CIs. ***D***, Time series of maximum head turns of P8 mice that received a bilateral intraocular injection of either saline (black traces) or SCH23390 (orange traces), as a function of irradiance. ***E***, Comparison of head turns for the saline or SCH23390-injected mice in ***D***. Horizontal lines indicate medians. Wilcoxon rank-sum test: $p = 0.37$, 1.00, 0.75, and 0.85 for comparisons of head turns on dark, 6 log unit, 7 log unit, and 9 log unit trials, respectively. $n = 11$ saline-injected mice and 14 SCH23390-injected mice.

retinal wave-triggered averages were significantly larger than noise fluctuations (determined by bootstrapping nonwave fluorescence changes; see Materials and Methods) were classified as participating in retinal waves. Finally, we functionally classified cells based on their light-evoked Ca^{2+} transients, and independently identified M1s from their anatomy, as described above. While all LST cells (20 of 20) and LSS cells (5 of 5) and most MS cells (15 of 16) participated in retinal waves, we found that only 50% of anatomically identified M1s (8 of 16 in total; 2 of 6 identified via melanopsin immunostaining and 6 of 10 identified in *Opn4::eGFP* retinas) participated (Fig. 6*F*; for a representative imaging session, see http://fellerlab.squarespace.com/movies). M1s thus had strikingly low rates of wave participation relative to other light-sensitive cells (>98% of MS, LST, and LSS) and the broader population of light-insensitive cells (~94%; 156 of 166 cells). Together, these results indicate that M1 ipRGCs are among the few cells in the GCL that are weakly depolarized by retinal waves.

We next compared the size of depolarizations induced by waves with those induced by light stimulation by comparing the magnitude of Ca^{2+} responses (ΔF/F; Fig. 6*G*). To test for differences in wave and light-evoked responses in cells of each functional cluster, we defined a light selectivity index (the ratio of the Ca^{2+} response evoked by light less the Ca^{2+} response evoked by waves, divided by their sum). Indeed, M1/HS and MS cells had smaller response to waves than light, in contrast to LST, which had the opposite, and LSS cells which had similar responses (Fig. 6*H*). While the properties of retinal waves in the *TrpC 6/7* KO were indistinguishable from control (Fig. 6*I–K*), light-responsive cells had significantly smaller light selectivity indices at all light intensities (Fig. 6*L*), consistent with the loss of photosensitivity we observed in M1/HS cells (Fig. 2). Thus, M1 ipRGCs exhibit larger Ca^{2+} responses to light than retinal waves, and this functional specialization is disrupted in the *TrpC 6/7* KO.

Discussion

Photoaversion is an innate behavior that is present early in development, before maturation of the circuits that mediate image-

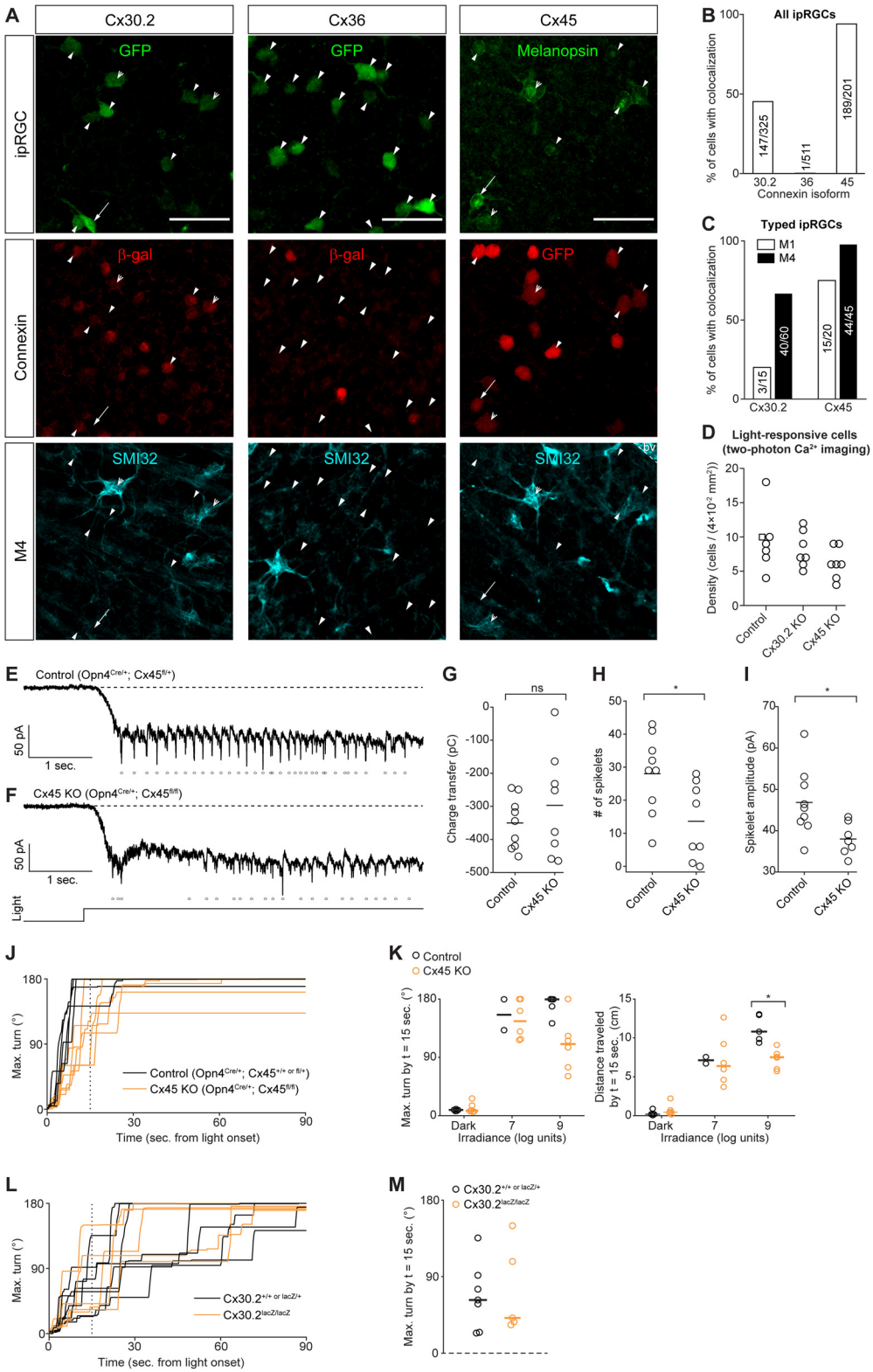

Figure 5. Connexin expression, role in ipRGC photosensitivity, and contribution to photoaversion. ***A***, Immunohistochemistry images indicating expression of Cx30.2 (left column), Cx36 (middle column), and Cx45 (right column) in ipRGC types. Connexin expression was visualized using transgenic mouse lines (Opn4::eGFP Cx30.2$^{lacZ/+}$, Opn4::eGFP Cx36$^{lacZ/+}$, and Opn4$^{Cre/+}$ Cx45$^{fl/+}$) that express *lacZ* and *GFP* in place of the genes encoding Cx30.2, Cx36, and Cx45, respectively. Open arrowheads indicate M4 ipRGCs (GFP^{+} or melanopsin^{+} and SMI32^{+}). Arrows indicate M1 ipRGCs (dendritic stratification in the outermost OFF layer of the inner plexiform layer). Closed arrowheads indicate ipRGCs of unknown type. Scale bar, 50 µm. bv, Blood vessel labeled by the anti-mouse secondary antibody used to detect SMI32 (see Materials and Methods). ***B***, Bar graph represents the proportions of ipRGCs with colocalized markers for connexin expression. The number of cells is indicated within each bar. $N = 2$ Opn4::eGFP Cx30.2$^{lacZ/+}$ mice, 2 Opn4::eGFP Cx36$^{lacZ/+\text{ or }lacZ/lacZ}$ mice, and 3 Opn4$^{Cre/+}$ Cx45$^{fl/+}$ mice. ***C***, Same as in ***B***, but for ipRGCs identifiable as M1 or M4. ***D***, The density of light-responsive cells in *ex vivo* retinas was not significantly affected by genetic deletion of Cx30.2 or Cx45. Each point represents one FOV from a two-photon population Ca^{2+} imaging experiment. Light stimuli ($\lambda_{max} = 420$ nm) were a series of 30 s pulses from 3.7 to 7.2 log units, identical to those used by us previously (Caval-Holme et al., 2019). Control: retinas from WT mice of genetic backgrounds matched to the Cx30.2 KO and Cx45 KO. $N = 6$ FOV from 2 Opn4::eGFP mice and 1 Opn4$^{Cre/+}$ Cx45$^{fl/+}$ mouse (square symbol; one copy of the Opn4 gene is replaced with

forming vision. Here we report that the behavior is reduced in mice lacking the TRPC6/7 phototransduction mechanism and is normal in mice with reduced gap junction coupling and in mice in which all ipRGCs other than the Brn3b-negative M1s are ablated. Two-photon calcium imaging in isolated retinas confirmed that TRPC6/7 KO reduces light responses specifically in M1 ipRGCs. In addition, we discovered that M1s are weakly depolarized by retinal waves, providing a potential cue by which the brain distinguishes M1 depolarizations induced by light from those induced by retinal waves. Together, these data indicate that M1s provide a dedicated pathway for photoaversion during development.

Brn3b-negative M1 ipRGCs are the principal drivers of photoaversion

Our data are consistent with a functional organization in which M1 ipRGCs, specifically the subset lacking expression of the Brn3b transcription factor, drive photoaversion. The evidence for this is several-fold: First, we found that the threshold light intensity required to elicit photoaversion is bright enough to activate M1 and M3 ipRGCs (M3s do not tile the retina with their dendritic arbors, suggesting they may not constitute a defined RGC type) (Berson et al., 2010; Schmidt and Kofuji, 2011) but too dim to activate M2, M4, M5, and M6 ipRGCs (the light intensity threshold for M4s is low in the adult) (Sonoda et al., 2018). Second, genetic deletion of TRPC6 and TRPC7 ion channels, which mediate light responses primarily in M1 ipRGCs in the adult (Jiang et al., 2018; Sonoda et al., 2018), dramatically reduced photoaversion and diminished photosensitivity in *ex vivo* M1s but had little effect on photosensitivity in other ipRGCs. Third, $Opn4^{Cre}$ $Brn3b^{DTA}$ mice, in which all ipRGCs save for ~400 Brn3b-negative M1s are ablated, had apparently normal photoaversion. Fourth, intraocular injections of drugs that modulate the extent of gap junction coupling, primarily affecting the light sensitivity of M2-M6 ipRGCs (Caval-Holme et al., 2019), had no effect on photoaversion. Similarly, genetic KO of connexins expressed in ipRGCs did not affect photoaversion at threshold light intensities. Finally, we found that M1s have limited depolarizations by retinal waves, a property that may make them uniquely well suited to the requirements of photoaversion behavior.

Do M2-M6 contribute to photoaversion at saturating intensities? While *TrpC 6/7* KO mice exhibited no response to a near-threshold light intensity, they made small head turns in response to saturating intensities (Fig. 1). This observation implies either a contribution from M2-M6 or residual signaling from M1s, consistent with small Ca^{2+} (Fig. 2) and current (Jiang et al., 2018) responses measured in *TrpC 6/7* KO M1s. Mice lacking Cx45 in ipRGCs (Fig. 5) exhibited reduced spikelets in M4 ipRGCs and slightly reduced photoaversion at saturating intensities. (In mice that had received an intraocular injection of MFA, there was no detectable reduction in photoaversion. This is likely because of highly variable behavior in mice that receive intraocular injections, which leads to irregular and prolonged pupillary constriction.)

The identification of M1s as primary sensory neurons for photoaversion aligns with results of previous studies of the brain areas involved in light's aversive aspects. In neonatal rodents, neurons in the amygdala and posterior thalamus express c-Fos following aversive light stimuli (Delwig et al., 2012), and one study found that lesions involving the superior colliculus abolished photoaversion (Routtenberg et al., 1978). In adult mice, ipRGC input to the peri-habenula drives the negative effects of light on mood (Fernandez et al., 2018; An et al., 2020). All these regions receive anatomic projections from M1 ipRGCs (Do, 2019). Our finding that Brn3b-DTA pups exhibit normal photoaversion (Fig. 3) further limits potential brain areas that mediate this behavior. In adult Brn3b-DTA mice, the primary ipRGC (Brn3b-negative M1s) projection is to the suprachiasmatic nucleus (Chen et al., 2011; Li and Schmidt, 2018). However, the surviving ipRGCs in these mice make limited projections to two regions implicated above: the superior colliculus and peri-habenula, among others (Li and Schmidt, 2018). While the canonical function of projections to the suprachiasmatic nucleus is light entrainment of the circadian clock, there is evolutionary precedent for overlapping function. For example, in larval *Drosophila*, projections from the eye to the circadian pacemaker neurons also relay light information for photoaversion (Mazzoni et al., 2005).

Identification of connexins in developing ipRGCs

In the adult retina, the coupling patterns of ipRGCs are well described. ipRGCs are coupled to several types of amacrine cells (Müller et al., 2010; Reifler et al., 2015; Pottackal et al., 2021), many of which fire action potentials (Reifler et al., 2015). Coupling between ipRGCs has not been observed. Cx36 has been implicated in ipRGC-AC coupling (Harrison et al., 2021) and a subset of ipRGCs express Cx30.2 (Meyer et al., 2016). Cx45 is only thought to be present in bistratified RGCs in the adult (Schubert et al., 2005), and thus could be present in M3s.

The coupling pattern and connexin expression during development are distinct from the adult. M2-M6 ipRGCs are extensively coupled during development, and this strongly contributes to the light response (Arroyo et al., 2016; Caval-Holme et al., 2019). In contrast to the adult (Harrison et al., 2021), we found little evidence for Cx36 expression in ipRGCs during development (Fig. 5), consistent with previous work from our laboratory showing that Cx36 expression

←

Cre, as in the Cx45 KO). Cx30.2 KO: 7 FOV from 2 mice. Cx45 KO: 7 FOV from 3 mice. One-way ANOVA ($F = 1.88$, 2 degrees of freedom, $p = 0.18$). ***E***, Voltage-clamp recording of light-evoked current in an M4 ipRGC in the *ex vivo* retina of a Cx45 heterozygote ($Opn4^{Cre/+}$ $Cx45^{fl/+}$) mouse. Dashed line indicates holding current reference. Points represent detected spikelets (inward currents magnitude > 30 pA). Illumination ($\lambda_{max} = 420$ nm, irradiance = 10^8 photons μm^{-2} s^{-1}) lasted for 5 s. Light monitor below ***F***. Cells were held at −80 mV. The internal solution contained QX314 (5 mM), a voltage-gated sodium channel antagonist. Recording solution contained 50 μM D-AP5, 20 μM DNQX, and 8 μM DHβE (for further details, see Caval-Holme et al., 2019). ***F***, Same as in ***E***, except that the cell was from a littermate Cx45 KO ($Opn4^{Cre/+}$ $Cx45^{fl/+}$) mouse recorded on the same day as the cell in ***E***. ***G***, Comparison of light-evoked charge transfer (pico-coulombs) in M4 ipRGCs from Cx45 Hets and Cx45 KOs. Horizontal lines indicate medians. $p = 0.67$ (Wilcoxon rank-sum test). Cx45 Het: $n = 9$ cells from 4 mice. Cx45 KO: $n = 8$ cells from 3 mice. ***H***, Comparison of the number of light-evoked spikelets in M4 ipRGCs from Cx45 Hets and Cx45 KOs. Horizontal lines indicate medians. $^*p < 0.05$ (Wilcoxon rank-sum test). Same cells as in ***G***. ***I***, Comparison of the amplitude of light-evoked spikelets in M4 ipRGCs from Cx45 Hets and Cx45 KOs. Horizontal lines indicate medians. $^*p < 0.05$ (Wilcoxon rank-sum test). Same cells as in ***G*** and ***H***, with one Cx45 KO cell excluded as it had no spikelets. ***J***, Time series of maximum head turns of P8 Control ($Opn4^{Cre/+}$ $Cx45^{+/+}$ or $Opn4^{Cre/+}$ $Cx45^{fl/+}$; black traces) and Cx45 KO (yellow traces; $Opn4^{Cre/+}$ $Cx45^{fl/fl}$) mice. ***K***, Comparison of head turns (left) and travel distance (right) in P8 genetic control ($Opn4^{Cre/+}$ and $Opn4^{Cre/+}$ $Cx45^{fl/+}$ littermates) and Cx45 KO ($Opn4^{Cre/+}$ $Cx45^{fl/fl}$) mice. Control: $n = 3$ $Opn4^{Cre/+}$ and 2 $Opn4^{Cre/+}$ $Cx45^{fl/+}$. Cx45 KO: $n = 6$. $^*p < 0.05$ (Wilcoxon rank-sum test). Error bars indicate medians. ***L***, Time series of maximum head turns of P7 Control (black traces; $Cx30.2^{+/+ \text{ or } lacZ/+}$) and Cx30.2 KO (yellow traces; $Cx30.2^{lacZ/lacZ}$) mice. Light stimulus intensity was 10^9 photons μm^{-2} s^{-1}. ***M***, Comparison of the maximum head turn 15 s after light onset. Error bars indicate medians. Same mice as in ***A***. $N = 7$ Control mice and 5 Cx30.2 KO mice.

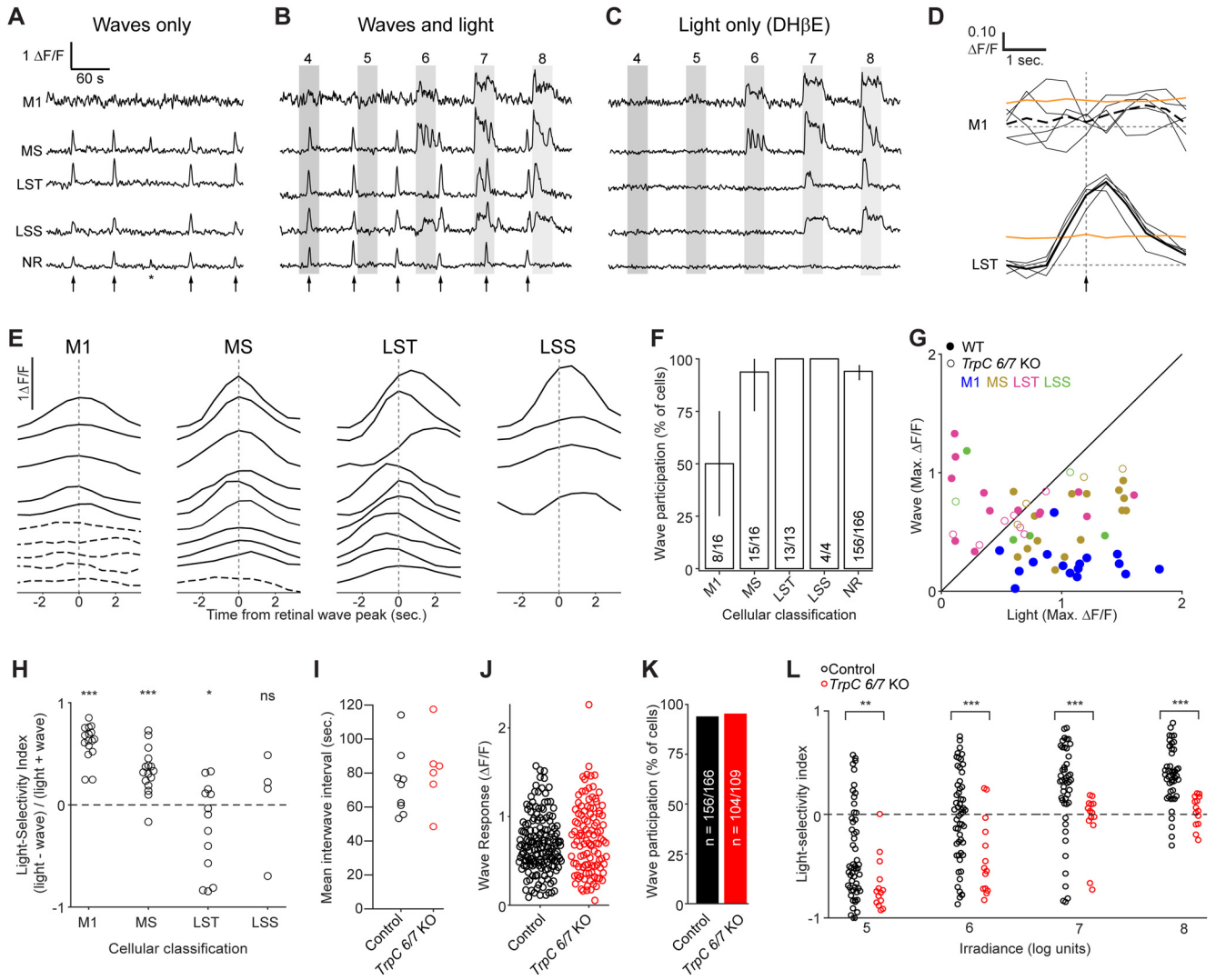

Figure 6. M1 ipRGCs are weakly depolarized by retinal waves. ***A-C***, Example ΔF/F traces from the same cells under a series of imaging conditions: ***A***, Waves only. ***B***, Waves and light stimulation. ***C***, Light stimulation only (with waves blocked by DHβE). Arrows indicate timing of waves. Asterisk indicates a wave that involved only a portion of the FOV and was excluded from the analysis. Gray boxes represent duration of light stimuli (λ_{max} = 470 nm; 10^4-10^8 photons μm^{-2} s^{-1}). Waves-only and light-only traces were analyzed further. MS, LST, and LSS: functional cluster assignments based on each cell's light response (Fig. 2). NR: a randomly selected neuron within the ganglion cell layer that was not responsive to light. ***D***, Sample wave-triggered averages for two of the cells in ***A-C***. Thin black lines indicate epochs used to generate the wave-triggered average (thick black lines). Orange lines indicate 95th percentiles of distributions of averages triggered from random nonwave locations. Vertical dashed line indicates the timing of the population wave peak. Top, M1 cell (average trace shown as dashed line) did not exceed the 95th percentile at any point and was therefore defined as exempt from waves. Bottom, The LST cell clearly participates in waves. ***E***, Representative wave-triggered average traces, vertically offset for clarity. Cells are a subset of those in Figure 2. Dashed lines indicate a lack of wave participation. M1: anatomically identified M1 ipRGCs. ***F***, Proportions of light-responsive (M1, MS, LST, and LSS) and nonresponsive (NR) cells that participated in waves. $N = 9$ imaging FOV from 4 mice (1:1 C129:C57BL6/J or Opn4::eGFP). Cell counts indicated within the bar chart. Error bars indicate bootstrapped 95% CIs. ***G***, Maximum ΔF/F responses of individual ipRGCs to waves plotted against maximum responses to light (10^7 photons μm^{-2} s^{-1}). Each point represents one cell and is color-coded according to functional cluster assignment, based on the cell's light response (Fig. 2). *N* values for cells from Control mice (closed circles) are given in ***F***. For *TrpC 6/7* KO (open circles), $n = 1$ M1, 4 MS, 8 LST, 2 LSS cells from 5 imaging FOV from 2 mice. ***H***, Light selectivity index (calculated as 1 – (W/L), L being the maximum ΔF/F response of a cell to light stimulus and W being the maximum response to waves) for cells from the functional clusters defined in Figure 2. Light intensity: 10^7 photons μm^{-2} s^{-1}. Only the light-responsive cells from WT mice are shown. $^*p < 0.05$; $^{***}p < 0.0005$; Student's *t* test with Bonferroni correction. Not significant ($p = 0.22$). *N* values are given in ***F***. ***I***, Average interwave time intervals from different FOV in retinas from Control and *TrpC 6/7* KO mice. $p = 0.52$ (two-sample *t* test). ***J***, The distributions of ΔF/F responses to retinal waves were not significantly different between non–light-responsive cells from Control and *TrpC 6/7* KO retinas ($p = 0.13$, two-sample *t* test). ***K***, The proportion of non–light-responsive cells participating in retinal waves was indistinguishable between Control and *TrpC 6/7* KO retinas ($p = 0.61$, χ^2 test). ***L***, Light selectivity index in Control (1:1 C129:C57BL6/J; $n = 9$ FOV from 3 mice) and *TrpC 6/7* KO ($n = 6$ FOV from 2 mice) retinas, at four different light intensities. $^{**}p < 0.005$; $^{***}p < 0.0005$; Wilcoxon rank-sum test with Bonferroni correction.

in the ganglion cell layer is low during the first postnatal week (Hansen et al., 2005). We found a small percentage of ipRGCs to express Cx30.2 (Fig. 5), consistent with coupling described in the adult. Finally, we discovered that ipRGCs express Cx45 during development. It is important to note that Cx45 expression was determined using an intersectional transgenic approach; thus, expression of Cx45 at any point in development will lead to expression of GFP. In contrast, Cx30.2 and Cx36 expression was assessed based on expression of β-galactosidase, which will reflect the

level of expression only at the age at which we did the experiment. That said, Cx45 KO mice had a physiological phenotype, with M4-ipRGCs displaying fewer spikelets than observed in control animals (Fig. 5*E*,*F*). This provides a potential basis for M4s contributing to photoaversion at saturating intensities.

Why don't retinal waves interfere with photoaversion?

Previously, it was assumed that all RGCs, including ipRGCs, participate in waves because of their ubiquitous expression of nicotinic AChRs (Aizenman et al., 1990; Zoli et al., 1995) and the volume release of acetylcholine by starburst amacrine cells (Ford et al., 2012). However, a recently published single-cell transcriptomics dataset revealed that M1 ipRGCs express strikingly low levels of genes encoding nicotinic AChR subunits (Tran et al., 2019). We found that M1 ipRGCs exhibited depolarizations induced by light stimulation that were stronger than those induced by retinal waves, with about half of anatomically identified M1 ipRGCs exhibiting no detectable calcium transient in response to waves (Fig. 6).

In addition to the strength of depolarization, there are other differences between retinal wave-evoked and light-evoked activity in RGCs that could be used by the ipRGC-recipient regions of the brain to discriminate the two sources of input. Light stimuli induce synchronous depolarizations lasting for 10s of seconds while retinal waves induce propagating depolarizations lasting 1-2 s per RGC (Meister et al., 1991; Ford et al., 2012). Light stimuli can also activate ipRGCs across the entire retina, while retinal waves have finite propagation (Feller et al., 1996). Although we have not explored the full temporal and spatial properties of visual stimuli that evoke photoaversion, M1s integrate photons over large ranges of stimulus duration and generate prolonged responses to brief light stimuli (Emanuel and Do, 2015), including single photon absorptions (Do et al., 2009). Hence duration of depolarization and the number of simultaneously depolarized neurons may be other features that allow the brain to differentiate light-evoked and spontaneous activity. Nevertheless, our observation of strikingly weak responses of M1 ipRGCs to waves suggests that the nervous system has evolved to minimize inputs from spontaneous activity to the information channels subserving photoaversion. Exemption from retinal waves may also underlie the absence of retinotopic and eye-specific refinement observed in retinorecipient regions receiving predominantly M1 projections (Ecker et al., 2010), increasing the extent of light's spatial integration in non–image-forming pathways.

In conclusion, M1 ipRGCs constitute a distinct information channel that mediates photoaversion during the period of early postnatal development when retinal waves drive activity-dependent refinement of retinal projections to the brain.

References

Ackman JB, Burbridge TJ, Crair MC (2012) Retinal waves coordinate patterned activity throughout the developing visual system. Nature 490:219–225.

Aizenman E, Loring RH, Lipton SA (1990) Blockade of nicotinic responses in rat retinal ganglion cells by neuronal bungarotoxin. Brain Res 517:209–214.

Allen AE, Storchi R, Martial FP, Petersen RS, Montemurro MA, Brown TM, Lucas RJ (2014) Melanopsin-driven light adaptation in mouse vision. Curr Biol 24:2481–2490.

An K, Zhao H, Miao Y, Xu Q, Li YF, Ma YQ, Shi YM, Shen JW, Meng JJ, Yao YG, Zhang Z, Chen JT, Bao J, Zhang M, Xue T (2020) A circadian rhythm-gated subcortical pathway for nighttime-light-induced depressive-like behaviors in mice. Nat Neurosci 23:869–880.

Aranda M, Schmidt T (2021) Diversity of intrinsically photosensitive retinal ganglion cells: circuits and functions. Cell Mol Life Sci 78:889–907.

Arroyo DA, Kirkby LA, Feller MB (2016) Retinal waves modulate an intraretinal circuit of intrinsically photosensitive retinal ganglion cells. J Neurosci 36:6892–6905.

Baden T, Berens P, Franke K, Román Rosón M, Bethge M, Euler T (2016) The functional diversity of retinal ganglion cells in the mouse. Nature 529:345–350.

Bansal A, Singer JH, Hwang BJ, Xu W, Beaudet A, Feller MB (2000) Mice lacking specific nicotinic acetylcholine receptor subunits exhibit dramatically altered spontaneous activity patterns and reveal a limited role for retinal waves in forming ON and OFF circuits in the inner retina. J Neurosci 20:7672–7681.

Berson DM, Castrucci AM, Provencio I (2010) Morphology and mosaics of melanopsin-expressing retinal ganglion cell types in mice. J Comp Neurol 518:2405–2422.

Blankenship AG, Feller MB (2010) Mechanisms underlying spontaneous patterned activity in developing neural circuits. Nat Rev Neurosci 11:18–29.

Blankenship AG, Ford KJ, Johnson J, Seal RP, Edwards RH, Copenhagen DR, Feller MB (2009) Synaptic and extrasynaptic factors governing glutamatergic retinal waves. Neuron 62:230–241.

Blankenship AG, Hamby AM, Firl A, Vyas S, Maxeiner S, Willecke K, Feller MB (2011) The role of neuronal connexins 36 and 45 in shaping spontaneous firing patterns in the developing retina. J Neurosci 31:9998–10008.

Caval-Holme F, Zhang Y, Feller MB (2019) Gap junction coupling shapes the encoding of light in the developing retina. Curr Biol 29:4024–4035.e5.

Chen SK, Badea TC, Hattar S (2011) Photoentrainment and pupillary light reflex are mediated by distinct populations of ipRGCs. Nature 476:92–95.

Chew KS, VanDunk C, Vicarel DC, Tufford A, Weng S, Gray PA, Cayouette M, Herzog ED, Zhao H, Berson DM, Hattar S (2017) A subset of ipRGCs regulates both maturation of the circadian clock and segregation of retinogeniculate projections in mice. Elife 6:e22861.

Deans MR, Gibson JR, Sellitto C, Connors BW, Paul DL (2001) Synchronous activity of inhibitory networks in neocortex requires electrical synapses containing connexin36. Neuron 31:477–485.

Delwig A, Logan AM, Copenhagen DR, Ahn AH (2012) Light evokes melanopsin-dependent vocalization and neural activation associated with aversive experience in neonatal mice. PLoS One 7:e43787.

Delwig A, Majumdar S, Ahern K, Lavail MM, Edwards R, Hnasko TS, Copenhagen DR (2013) Glutamatergic neurotransmission from melanopsin retinal ganglion cells is required for neonatal photoaversion but not adult pupillary light reflex. PLoS One 8:e83974.

Delwig A, Margolis T, Copenhagen DR (2018) Melanopsin expression in the cornea. Vis Neurosci 35:E004.

Do MT (2019) Melanopsin and the intrinsically photosensitive retinal ganglion cells: biophysics to behavior. Neuron 104:205–226.

Do MT, Yau KW (2013) Adaptation to steady light by intrinsically photosensitive retinal ganglion cells. Proc Natl Acad Sci USA 110:7470–7475.

Do MT, Kang SH, Xue T, Zhong H, Liao HW, Bergles DE, Yau KW (2009) Photon capture and signalling by melanopsin retinal ganglion cells. Nature 457:281–287.

Ecker JL, Dumitrescu ON, Wong KY, Alam NM, Chen SK, LeGates T, Renna JM, Prusky GT, Berson DM, Hattar S (2010) Melanopsin-expressing retinal ganglion-cell photoreceptors: cellular diversity and role in pattern vision. Neuron 67:49–60.

Emanuel AJ, Do MT (2015) Melanopsin tristability for sustained and broadband phototransduction. Neuron 85:1043–1055.

Feller MB, Wellis DP, Stellwagen D, Werblin FS, Shatz CJ, Feller MB, Wellis DP, Stellwagen D, Werblin FS, Shatz CJ (1996) Requirement for

cholinergic synaptic transmission in the propagation of spontaneous retinal waves. Science 272:1182–1187.
Feller MB, Butts DA, Aaron HL, Rokhsar DS, Shatz CJ (1997) Dynamic processes shape spatiotemporal properties of retinal waves. Neuron 19:293–306.
Fernandez DC, Berson DM, Hattar S (2018) Light affects mood and learning through distinct retina-brain pathways. Cell 175:71–84.e18.
Ford KJ, Félix AL, Feller MB (2012) Cellular mechanisms underlying spatiotemporal features of cholinergic retinal waves. J Neurosci 32:850–863.
Güler AD, Hankins MW, Berson DM, Lucas RJ, Yau KW, Hattar S (2008) Melanopsin cells are the principal conduits for rod–cone input to non–image-forming vision. Nature 453:102–105.
Hansen KA, Torborg CL, Elstrott J, Feller MB (2005) Expression and function of the neuronal gap junction protein connexin 36 in developing mammalian retina. J Comp Neurol 493:309–320.
Harrison KR, Chervenak AP, Resnick SM, Reifler AN, Wong KY (2021) Amacrine cells forming gap junctions with intrinsically photosensitive retinal ganglion cells: ipRGC types, neuromodulator contents, and connexin isoform. Vis Neurosci 62:1–9.
Hoon M, Okawa H, Della Santina L, Wong RO (2014) Functional architecture of the retina: development and disease. Prog Retin Eye Res 42:44–84.
Jiang Z, Yue WW, Chen L, Sheng Y, Yau KW (2018) Cyclic-nucleotide- and HCN-channel-mediated phototransduction in intrinsically photosensitive retinal ganglion cells. Cell 175:652–664.e12.
Johnson J, Wu V, Donovan M, Majumdar S, Rentería RC, Porco T, van Gelder RN, Copenhagen DR (2010) Melanopsin-dependent light avoidance in neonatal mice. Proc Natl Acad Sci USA 107:17374–17378.
Jones KA, Hatori M, Mure LS, Bramley JR, Artymyshyn R, Hong SP, Marzabadi M, Zhong H, Sprouse J, Zhu Q, Hartwick ATE, Sollars PJ, Pickard GE, Panda S (2013) Small-molecule antagonists of melanopsin-mediated phototransduction. Nat Chem Biol 9:630–635.
Kaplan HJ, Chiang CW, Chen J, Song SK (2010) Vitreous volume of the mouse measured by quantitative high-resolution MRI. Invest Ophthalmol Vis Sci 51:4414.
Kirkby LA, Feller MB (2013) Intrinsically photosensitive ganglion cells contribute to plasticity in retinal wave circuits. Proc Natl Acad Sci USA 110:12090–12095.
Kreuzberg MM, Schrickel JW, Ghanem A, Kim JS, Degen J, Janssen-Bienhold U, Lewalter T, Tiemann K, Willecke K (2006) Connexin30.2 containing gap junction channels decelerate impulse propagation through the atrioventricular node. Proc Natl Acad Sci USA 103:5959–5964.
Li JY, Schmidt TM (2018) Divergent projection patterns of M1 ipRGC subtypes. J Comp Neurol 526:2010–2023.
Lucas JA, Schmidt TM (2019) Cellular properties of intrinsically photosensitive retinal ganglion cells during postnatal development. Neural Dev 14:8.
Matynia A, Parikh S, Chen B, Kim P, McNeill DS, Nusinowitz S, Evans C, Gorin MB (2012) Intrinsically photosensitive retinal ganglion cells are the primary but not exclusive circuit for light aversion. Exp Eye Res 105:60–69.
Matynia A, Nguyen E, Sun X, Blixt FW, Parikh S, Kessler J, Pérez de Sevilla Müller L, Habib S, Habib S, Kim P, Wang ZZ, Rodriguez A, Charles A, Nusinowitz S, Edvinsson L, Barnes S, Brecha NS, Gorin MB (2016) Peripheral sensory neurons expressing melanopsin respond to light. Front Neural Circuits 10:60.
Maxeiner S, Dedek K, Janssen-Bienhold U, Ammermüller J, Brune H, Kirsch T, Pieper M, Degen J, Krmüger O, Willecke K, Weiler R. (2005) Deletion of connexin45 in mouse retinal neurons disrupts the rod/cone signaling pathway between AII amacrine and ON cone bipolar cells and leads to impaired visual transmission. J Neurosci 25:566–576.
Mazzoni EO, Desplan C, Blau J (2005) Circadian pacemaker neurons transmit and modulate visual information to control a rapid behavioral response. Neuron 45:293–300.
McAdams H, Kaiser EA, Igdalova A, Haggerty EB, Cucchiara B, Brainard DH, Aguirre GK (2020) Selective amplification of ipRGC signals accounts for interictal photophobia in migraine. Proc Natl Acad Sci USA 117:17320–17329.
Meister M, Wong RO, Baylor DA, Shatz CJ (1991) Synchronous bursts of action potentials in ganglion cells of the developing mammalian retina. Science 252:939–943.
Meyer A, Tetenborg S, Greb H, Segelken J, Dorgau B, Weiler R, Hormuzdi SG, Janssen-Bienhold U, Dedek K (2016) Connexin30.2: in vitro interaction with Connexin36 in HeLa cells and expression in AII amacrine cells and intrinsically photosensitive ganglion cells in the mouse retina. Front Mol Neurosci 9:36.
Mooney R, Penn AA, Gallego R, Shatz CJ (1996) Thalamic relay of spontaneous retinal activity prior to vision. Neuron 17:863–874.
Müller LP, Do MT, Yau KW, He S, Baldridge WH (2010) Tracer coupling of intrinsically photosensitive retinal ganglion cells to amacrine cells in the mouse retina. J Comp Neurol 518:4813–4824.
Mure LS, Hatori M, Ruda K, Benegiamo G, Demas J, Panda S (2018) Sustained melanopsin photoresponse is supported by specific roles of β-arrestin 1 and 2 in deactivation and regeneration of photopigment. Cell Rep 25:2497–2509.e4.
Nath T, Mathis A, Chen AC, Patel A, Bethge M, Mathis MW (2019) Using DeepLabCut for 3D markerless pose estimation across species and behaviors. Nat Protoc 14:2152–2176.
Noseda R, Kainz V, Jakubowski M, Gooley JJ, Saper CB, Digre K, Burstein R (2010) A neural mechanism for exacerbation of headache by light. Nat Neurosci 13:239–245.
Noseda R, Copenhagen D, Burstein R (2019) Current understanding of photophobia, visual networks and headaches. Cephalalgia 39:1623–1634.
Perez-Leighton CE, Schmidt TM, Abramowitz J, Birnbaumer L, Kofuji P (2011) Intrinsic phototransduction persists in melanopsin-expressing ganglion cells lacking diacylglycerol-sensitive TRPC subunits. Eur J Neurosci 33:856–867.
Pottackal J, Walsh HL, Rahmani P, Zhang K, Justice NJ, Demb JB (2021) Photoreceptive ganglion cells drive circuits for local inhibition in the mouse retina. J Neurosci 41:1489–1504.
Reifler AN, Chervenak AP, Dolikian ME, Benenati BA, Li BY, Wachter RD, Lynch AM, Demertzis ZD, Meyers BS, Abufarha FS, et al. (2015) All spiking, sustained ON displaced amacrine cells receive gap-junction input from melanopsin ganglion cells. Curr Biol 25:2763–2773.
Routtenberg A, Strop M, Jerdan J (1978) Response of the infant rat to light prior to eyelid opening: mediation by the superior colliculus. Dev Psychobiol 11:469–478.
Rupp AC, Ren M, Altimus CM, Fernandez DC, Richardson M, Turek F, Hattar S, Schmidt TM (2019) Distinct ipRGC subpopulations mediate light's acute and circadian effects on body temperature and sleep. Elife 8:e44358.
Schmidt TM, Kofuji P (2011) Structure and function of bistratified intrinsically photosensitive retinal ganglion cells in the mouse. J Comp Neurol 519:1492–1504.
Schmidt TM, Taniguchi K, Kofuji P (2008) Intrinsic and extrinsic light responses in melanopsin-expressing ganglion cells during mouse development. J Neurophysiol 100:371–384.
Schubert T, Maxeiner S, Krüger O, Willecke K, Weiler R (2005) Connexin45 mediates gap junctional coupling of bistratified ganglion cells in the mouse retina. J Comp Neurol 490:29–39.
Semo M, Gias C, Ahmado A, Sugano E, Allen AE, Lawrence JM, Tomita H, Coffey PJ, Vugler AA (2010) Dissecting a role for melanopsin in behavioural light aversion reveals a response independent of conventional photoreception. PLoS One 5:e15009.
Shekhar K, Whitney IE, Butrus S, Peng YR, Sanes JR (2022) Diversification of multipotential postmitotic mouse retinal ganglion cell precursors into discrete types. Elife 11:e73809.
Sikka G, Hussmann GP, Pandey D, Cao S, Hori D, Park JT, Steppan J, Kim JH, Barodka V, Myers AC, Santhanam L, Nyhan D, Halushka MK, Koehler RC, Snyder SH, Shimoda LA, Berkowitz DE (2014) Melanopsin mediates light-dependent relaxation in blood vessels. Proc Natl Acad Sci USA 111:17977–17982.
Sonoda T, Lee K, Birnbaumer L, Schmidt TM (2018) Melanopsin phototransduction is repurposed by ipRGC subtypes to shape the function of distinct visual circuits. Neuron 99:754-767.
Stosiek C, Garaschuk O, Holthoff K, Konnerth A (2003) In vivo two-photon calcium imaging of neuronal networks. Proc Natl Acad Sci USA 100:7319–7324.

Tiriac A, Smith B, Feller MB (2018) Light prior to eye opening promotes retinal waves and eye-specific segregation. Neuron 100:1059–1065.e4.

Tran NM, Shekhar K, Whitney IE, Jacobi A, Benhar I, Hong G, Yan W, Adiconis X, Arnold ME, Lee JM, Levin JZ, Lin D, Wang C, Lieber CM, Regev A, He Z, Sanes JR (2019) Single-cell profiles of retinal neurons differing in resilience to injury reveal neuroprotective genes. Neuron 104:1039–1055.e12.

Tu DC, Zhang D, Demas J, Slutsky EB, Provencio I, Holy TE, Van Gelder RN (2005) Physiologic diversity and development of intrinsically photosensitive retinal ganglion cells. Neuron 48:987–999.

Weliky M, Katz C (1999) Correlational structure of spontaneous neuronal activity in the developing lateral geniculate nucleus in vivo. Science 285:599–604.

Wong WT, Myhr KL, Miller ED, Wong RO (2000) Developmental changes in the neurotransmitter regulation of correlated spontaneous retinal activity 20:351–360.

Xue T, Do MT, Riccio A, Jiang Z, Hsieh J, Wang HC, Merbs SL, Welsbie DS, Yoshioka T, Weissgerber P, Stolz S, Flockerzi V, Freichel M, Simon MI, Clapham DE, Yau KW (2011) Melanopsin signalling in mammalian iris and retina. Nature 479:67–72.

Zhang BB, Yao YY, Zhang HF, Kawakami K, Du JL (2017) Left habenula mediates light-preference behavior in zebrafish via an asymmetrical visual pathway. Neuron 93:914–928.e4.

Zoli M, Le Novère N, Hill JA, Changeux JP (1995) Developmental regulation of nicotinic ACh receptor subunit mRNAs in the rat central and peripheral nervous systems. J Neurosci 15:1912–1939.